RMetS

Royal Meteorological Society

Morphology of breeze circulations induced by surface flux heterogeneities and their impact on convection initiation

Nicolas Rochetin,* Fleur Couvreux and Françoise Guichard

CNRM, Météo-France and CNRS, Toulouse, France

*Correspondence to: N. Rochetin, Centre National de Recherche Meteorologique, Météo-France, 42 Avenue Gaspard Coriolis, 31057 Toulouse, France. E-mail: nicolas.rochetin@lmd.jussieu.fr

This study analyses the role of breeze circulations induced by a surface sensible heat flux heterogeneity on deep convection initiation. Large-eddy simulations are used to disentangle the processes at play in a typical case of daytime triggering of deep convection over a semi-arid land. We show that the presence of a realistic surface sensible heat flux heterogeneity leads to an earlier triggering of convection and induces a strong determinism in the triggering location at the beta-mesoscale (i.e. ~ 50 km). The transition to deep convection consists of three consecutive stages, each one corresponding to a specific mode of interaction between (i) the boundary-layer thermals (small-scale), (ii) the breeze circulation (mesoscale) and (iii) the background wind (synoptic scale). These stages are both interpreted thermodynamically and morphologically. All along the transition phase, the boundary-layer growth acts to slow down the background wind, which strengthens the breeze circulation. The breeze evolves towards a circular shape which optimizes moisture convergence and cloud formation just prior to triggering. The presence of wind shear leads with a more asymmetric shape of the breeze in the afternoon, associated with a preferential triggering on the down-shear side of the breeze circulation.

1. Introduction

Mesoscale circulations induced by surface sensible heat flux heterogeneities are important sources of vertical transport of heat, moisture and momentum (Pielke *et al.*, 1991; Segal and Arritt, 1992, SA92 below). Differential heating patterns at the β-mesoscale (i.e. from 20 to 200 km) generate horizontal surface pressure gradients (Lee and Kimura, 2001) which induce horizontal flows from cooler to warmer surfaces. Those breeze-like circulations, also named Non-classical Mesoscale Circulations (NCMCs; SA92), may interact with (i) small-scale turbulence and (ii) the larger-scale flow (SA92). Over land, breeze circulations can be onset by the presence of gradients of soil wetness, vegetation cover, surface albedo, or even cloudiness which typically arise over a large range of temporal scales (SA92; Pielke *et al.*, 1991; Dalu and Pielke, 1993; Chen and Avissar, 1994b). According to SA92, the pressure force that generates the breeze circulation scales with the mixed-layer height horizontal gradient which is induced by the differential heating at the surface. It is associated with stronger turbulence and higher thermals over the positive anomaly. This scaling suggests close links between small-scale planetary boundary-layer (PBL) turbulence and the mesoscale breeze circulation. In the Tropics, sensible heat fluxes can reach more than $300 \, \text{W} \, \text{m}^{-2}$ (Gounou *et al.*, 2012; Couvreux *et al.*, 2012) over dry soils and horizontal gradients of temperature in the boundary layer (BL) can reach several K over a few tens

of kilometres (SA92; Taylor *et al.*, 2007; Dixon *et al.*, 2013). Under a weak synoptic forcing, these local breeze circulations are able to initiate deep convection by creating convergence lines and localized rising motions beyond the level of free convection (Emori, 1998; Pielke, 2001; Birch *et al.*, 2015).

Depending on the atmospheric thermodynamic state, deep convection may be favoured either over moist soils or over dry soils (Findell and Eltahir, 2003). Over dry soils convective initiation will be favoured for a small potential temperature lapse rate above the PBL, i.e. for a less stable atmosphere within which the BL will grow fast. Here we focus on a semi-arid zone in the Sahel, a region that was highlighted as a 'Hot Spot' for soil-moisture–precipitation feedbacks by Koster *et al.* (2004). There, the BL is dry and often capped by a strong inversion layer, resulting in a significant Convective Inhibition (CIN); i.e. the atmospheric environment is particularly unfavourable to convective triggering. In addition, this region exhibits strong spatial variability in soil moisture as a result of scarse convective events which lead to large variability in surface fluxes, especially at the start of the monsoon season when the soils are still relatively dry. In this semi-arid area, convective precipitation generates transient (1–3 days; Lohou and Patton, 2014) but strong mesoscale patterns of surface soil moisture and surface fluxes which can easily drive mesoscale circulations. These surface patterns in turn are found to play an important role in the triggering of deep convective events (Taylor *et al.*, 2011, 2013). For instance, by combining different

satellite products in this region, Taylor *et al.* (2011) highlighted the role of mesoscale surface soil moisture gradients as a cause for deep convection initiation; in particular, they showed that convection was preferentially initiated over dryer soils at scales of 100−200 km and over warm/dry anomalies at smaller spatial scale, from 10 to 40 km, ahead of transitions from warm/cold boundaries aligned along the mean background wind, i.e. on the dry side of soil moisture gradients, downstream from the centre of the positive surface heat flux anomaly. Since convective triggering occurs on the dry (hot) side of the gradient, this corresponds to a negative feedback between soil moisture and precipitation at the mesoscale. A similar mechanism has also been proposed for precipitation over fishbone-like deforestation patterns in Amazonia by Roy (2009). A better understanding of the interactions between surface processes and atmospheric convection at the mesoscale thus appear as a key step to further understanding and modelling land−atmosphere feedbacks.

Key tools to study the interactions between surface flux heterogeneities and the atmosphere are high-resolution models such as (i) cloud-resolving models (CRMs; Emori, 1998; Stirling and Petch, 2004), (ii) large-eddy simulations (LESs; Patton *et al.*, 2005; Lohou and Patton, 2014) and (iii) direct numerical simulation (DNS; van Heerwaarden *et al.*, 2014). Both CRMs and LESs have been conducted with (Rieck *et al.*, 2014) and without (Garcia-Carreras *et al.*, 2011) land surface models. These studies all showed that, over periodic sensible heat flux patterns, convergence and upward transport of heat and moisture is optimum over hot patches (Chen and Avissar, 1994b,a; Lynn *et al.*, 1998; Cheng and Cotton, 2004; Stirling and Petch, 2004; Patton *et al.*, 2005; Garcia-Carreras *et al.*, 2011; Wang and Gillies, 2011; Rieck *et al.*, 2014, 2015). The size, intensity and curvature of the heterogeneities are all important ingredients as they control the gradient strength at the mesoscale. Those geometrical influences have been studied with linear models (Dalu *et al.*, 1991; Dalu and Pielke, 1993). Nevertheless, the size and strength of the heterogeneity must be large enough to generate a sufficiently strong pressure gradient otherwise small-scale turbulence will erase the PBL differences on the two sides of the gradient. A minimum patch size of 10−20 km (SA92; Dixon *et al.*, 2013) appears to be required in order to generate horizontal PBL gradients that are strong enough to allow for the development of mesoscale circulations. In many modelling studies, lateral boundary conditions are chosen periodic and the sensible heat flux anomaly occupies a significant fraction of the domain. Therefore, by definition of this particular boundary condition, the horizontal-mean vertical velocity profile is zero (because of mass conservation). Thus, if the sensible heat flux positive anomaly occupies a large fraction of the domain, the associated breeze circulation may interact with itself through the domain lateral boundaries. In other words, the convective mesoscale circulation wavelength is constrained by the ratio between the heterogeneity pattern and the domain size. In contrast with these previous simulations, we chose a specific distinct set-up, broadly guided by observations, which largely damps the numerical interactions of the breeze with itself. Indeed, we also use periodic lateral boundary conditions, but the surface heterogeneity only covers 7% of the study domain.

Recently, Rieck *et al.* (2014) analysed the effects of land surface heterogeneities on cloud size distribution and deep convection initiation using idealized surface heterogeneities. Here, we propose to extend this work to a semi-arid area using a set-up which is close to observations. The present study analyses how a surface heterogeneity pattern (created by an antecedent precipitation event) influences the time and location of a deep convection triggering event at the mesoscale with a LES. It aims at adding physical interpretations and explanations to the observational evidence raised by Taylor *et al.* (2011). The surface heterogeneity consists of a single circular hot patch of 30 km diameter centred in a 100 km × 100 km wide domain. The choice of the shape and magnitude of the warm patch is broadly

guided by the observations (cf. Figure 9 of Lothon *et al.*, 2011; Guichard *et al.*, 2012). This shape also resembles the composite surface anomaly obtained by Taylor *et al.* (2011). In this sense, the surface set-up is also more realistic than the academic cyclic patterns adopted by most previous studies (van Heerwaarden and Guerau de Arellano, 2008; Garcia-Carreras *et al.*, 2011; Huang and Margulis, 2013). Hereafter, we will investigate the interaction between three different scales of motion: (i) the BL thermals, (ii) the mesoscale breeze circulation and (iii) the background wind. Their relative contribution to the triggering process will be at the core of the study.

Section 2 presents the data and the methodology. Section 3 describes the diagnostics specifically developed to characterize separately the breeze circulation and the BL thermals. Section 4 presents an analysis of the thermodynamical and morphological properties of the breeze circulation until deep convection triggering. Section 5 proposes a physical interpretation of the interaction between (i) thermals, (ii) breeze and (iii) large-scale flow during the transition, and section 6 gives concluding remarks.

2. Methodology

2.1. The Niamey 10 July 2006 AMMA case-study

The case-study investigated is based on observations from the African Monsoon Multidisciplinary Analysis (AMMA) field campaign on 10 July 2006 at Niamey. A short-lived convective cell developed over Niamey at 1540 LT (local time = UTC + 1 h) and further propagated 300 km westward of its initiation (Lothon *et al.*, 2011). The convective system was observed during its initiation and mature stage by several ground-based instruments (radar, wind profiler and atmospheric soundings) and satellite data. This case-study concerns a typical case of transition to deep convection over semi-arid regions, as frequently observed in the Sahel in late spring and early summer before the onset of the monsoon (Dione *et al.*, 2014, showed it for the Niamey region). It is characterized by a very low (≈ 0.1) surface evaporative fraction (i.e the fraction of the latent heat flux over the total heat flux) and associated with a relatively high BL and cloud heights (about 2.5 km). During this pre-monsoon phase, the low-level water vapour is essentially provided by the southwestern monsoon flux.

At the surface, a circular positive surface temperature anomaly, ≈ 30 km wide, was observed over Niamey. The convection initiated at 1540 LT right above this hot patch (cf. Figure 9 of Lothon *et al.*, 2011). This hot patch emerged because of the cooling of the surroundings induced by the rainfall events that occurred the previous week. The resulting surface temperature gradient was large and reached about 1 K km^{-1} at the hot patch boundary. As shown by Taylor *et al.* (2011), such a heterogeneity can play a role in the triggering of deep convection. In the following, we detail the methodology used to analyse the role of this surface heterogeneity in this LES.

2.2. The LES model and the different simulations

2.2.1. Model description and set-up

The simulation uses the LES version of the Meso-NH non-hydrostatic model developed by Lafore *et al.* (1998). In the LES configuration, only small-scale turbulence parametrization is activated with a turbulence kinetic energy (TKE) prognostic scheme (Cuxart *et al.*, 2000) using a length-scale proportional to the grid size and limited by stability (Deardorff, 1980). The prognostic equations of the six water species (i.e. water vapour, liquid water, precipitation, graupel, snow and ice) are governed by a bulk one-moment mixed-phase microphysical scheme (Pinty and Jabouille, 1998) combining a three-class ice parametrization with a Kessler scheme for the warm processes.

The same set-up as Couvreux *et al.* (2012) is used here. The domain is $100 \times 100 \times 20$ km^3, with a horizontal resolution of

500 m and periodic lateral boundary conditions. One may contest that $\Delta x = 500$ m is not fine enough to resolve most of the turbulent structures. We ran one of the simulations with a grid spacing of $\Delta x = 200$ m and found, as did Couvreux *et al.* (2012), similar growth of the BL, deep convection initiation and rain rates for both simulations. The only difference is that shallow convection occurs slightly earlier with $\Delta x = 200$ m. The vertical grid is defined with 118 stretched vertical levels (Gal-Chen and Somerville, 1975) up to 20 km. The vertical resolution is finer than 50 m in the BL and up to 2000 m (with 43 levels below 2000 m) and coarser higher up (reaching 250 m at the top of the model) and the lowest level is at 10 m. Rayleigh damping is progressively applied above 17 km altitude to prevent spurious reflections from the upper boundary. A random potential temperature perturbation of 0.1 K is added to the horizontally homogeneous initial state at the lowest level in order to initiate turbulent motions, as is classically done in LES. Surface fluxes as well as radiative heating are prescribed, which prevents any surface/atmosphere and cloud/radiation coupling and simplifies the analysis of convective processes. The simulation lasts 12 h, from 0600 to 1800 LT, with a time step of $\Delta t = 1$ s. In the following, the different simulations are described.

2.2.2. The LES baseline simulation without surface heterogeneities (HOM)

The baseline simulation with homogeneous surface is referred to as HOM in the following and corresponds to the reference simulation of Couvreux *et al.* (2012). Initial thermodynamic and wind profiles, varying-in-time homogeneous surface latent and sensible heat fluxes are described in Couvreux *et al.* (2012). Large-scale advection, based on the AMMA-ECMWF reanalysis (Agustí-Panareda *et al.*, 2010) and observations is taken into account. The large-scale horizontal advection is composed of a cooling (0.3 K h^{-1} maximum) and moistening (0.3 g kg^{-1} h^{-1} maximum) tendency affecting only the low levels (below 3000 m) in the morning (the maximum is prescribed at 0600 LT and then linearly decreases down to zero at noon; Figure 6(b) and (c) of Couvreux *et al.*, 2012). A large-scale vertical velocity w_{LS} of 1.5 cm s^{-1} from 1200 to 1800 LT is prescribed below 5000 m to mimic the local ascent induced by the mesoscale convergence generated by surface heterogeneities (Figure 6(a) of Couvreux *et al.*, 2012). Moreover, a large-scale background wind profile is prescribed at the initial stage. It comprises a low-level monsoon flow beneath the African Easterly Jet (AEJ) as observed on that day (Figure 4(b) of Lothon *et al.*, 2011, and Figure 5(d) of Couvreux *et al.*, 2012). Time-varying profiles of the divergence of radiative fluxes are also prescribed and the Coriolis effect is ignored. With these conditions, the LES first cumulus appeared around 1120 LT and deep convection was triggered around 1630 LT, which is the time when surface precipitation reaches the surface. This simulation has been evaluated against numerous observations (radiosondes, radar, satellites, ceilometers) in Couvreux *et al.* (2012)) and correctly reproduces the growth of the boundary layer, the development of shallow cumulus and the initiation of deep convection observed that day.

2.2.3. The sensitivity experiments

The aim of this study is to understand the different processes at play that lead to afternoon convective triggering over a heated land in the presence of surface flux heterogeneities. Sensitivity experiments are conducted by considering an isolated circular patch of 30 km diameter that covers a small fraction ($\sim 7\%$) of the study domain in a way that a breeze circulation (i.e. with an ascending and a subsiding branch) is almost completely embedded into the study domain and thus does not interact much with itself through lateral periodic boundaries. Hence, it is possible to distinguish the breeze from the large-scale circulation as the wind at domain boundaries is almost unaffected by the breeze circulation.

Table 1. Name and characteristics of the different simulations.

	$\dfrac{\overline{\Phi_s}}{\overline{\Phi_{s,hom}}}$	$\dfrac{\Phi_{s,max}}{\Phi_{s,min}}$	w_{LS} $(z < 5\,\text{km}) > 0$	$(\overline{u}, \overline{v}) > 0$	Wind shear
HOM	1	1	Yes	Yes	Yes
STRONG	1	2	Yes	Yes	Yes
WEAK	1	1.3	Yes	Yes	Yes
STRONG W0	1	2	No	Yes	Yes
WEAK W0	1	1.3	No	Yes	Yes
STRONG UV0	1	2	Yes	No	No
HOM STRONG	1.4	1	Yes	Yes	Yes
STRONG NOSHEAR	1	2	Yes	Yes	No

$\overline{\Phi_s}$ is the domain-averaged sensible heat flux while $\Phi_{s,max}$ and $\Phi_{s,min}$ are respectively the domain maximum and minimum values of Φ_s.

In total, seven different simulations (Table 1) have been performed with varying surface heat flux anomalies (in addition to the baseline simulation), with or without the large-scale ascent and with or without the synoptic wind.

The first sensitivity experiment corresponds to the addition of a surface heterogeneity. An idealized circular positive anomaly of sensible heat flux of $D = 30$ km diameter is introduced at the centre of the domain while evaporation is homogeneous across the domain. Despite the presence of this positive anomaly, the domain-averaged time-varying sensible heat flux $\overline{\Phi_s}$ is the same as in the HOM run $\overline{\Phi_{s,hom}}$ (Table 1) to conserve the total energy input. The sensitivity to the anomaly strength is also of interest. The maximum sensible flux $\Phi_{s,max}$ at the centre of the patch will be either (i) twice the value of the minimum $\Phi_{s,min}$ outside the patch in the case of a strong anomaly (STRONG run; Table 1) or (ii) 1.3 times greater in the case of a weak anomaly (WEAK run; Table 1). Figure 1 displays horizontal cross-sections of the prescribed sensible heat flux. In the STRONG case, the imposed values reach 500 W m^{-2} while in the WEAK case the values reach 400 W m^{-2}. The STRONG anomaly is here voluntary exaggerated to (i) better reveal the breeze circulation and analyse the processes at play and (ii) verify the robustness of the conclusions in an extreme case. We recall that, even though the atmospheric conditions are quasi-realistic (i.e. the atmospheric forcing is built from the observations), there is no surface coupling, making this simulation idealized in a sense. The effect of removing the large-scale forcing (suffix W0; Table 1) is tested. The sensitivity of the breeze to the large-scale flow is simply assessed by removing the background wind and imposing a zero wind speed at initialization (suffix UV0; Table 1).

Moreover, to distinguish the breeze effect from the surface processes at play over the patch, another homogeneous case is run but with a sensible heat flux equal to the horizontally averaged one over the patch region in the STRONG case (HOM STRONG in Table 1).

Finally, a simulation without vertical wind shear is also performed in order to understand how it could potentially affect triggering time and location (STRONG NOSHEAR in Table 1). This is merely done by removing the AEJ and imposing a constant vertical wind profile of ~ 3 m s^{-1} for the wind above the PBL.

3. Definitions and notations

3.1. Breeze characterization

Here we detail the protocol used to define the breeze geometry. Since the breeze results from a pressure gradient at the mesoscale, we use the pressure anomaly field p' where $p = \overline{p} + p'$ (the overbar denotes an horizontal average over the whole domain) as a basis to define the breeze geometry. Indeed, p' depicts a departure from the hydrostatic mean pressure field and can be directly related to the mesoscale circulation streamlines. From now on, all anomalies x' will refer to spatial anomalies.
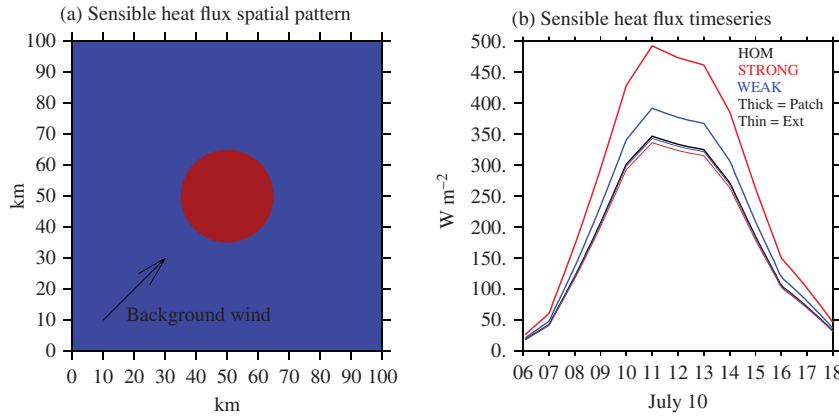
Figure 1. (a) Map of the sensible heat flux heterogeneity pattern. Surface evaporation is homogeneous across the domain. (b) Time series of sensible heat flux averaged over the patch (bold lines) and outside the patch (thin lines).

3.1.1. First estimate of the breeze height $h_{b,est}$

- We first compute the horizontally averaged pressure anomaly over the patch region $\overline{p'^{patch}}$.
- Then, we define the first estimate of the breeze height $h_{b,est}$ as the first altitude which verifies $\overline{p'^{patch}}(z_1 = h_{b,est}) = 0$. This altitude corresponds to the depth of the negative pressure anomaly relative to the positive heating anomaly experienced just over the hot patch.

3.1.2. Breeze dynamical definition

- The wind vector $\mathbf{U} = u\mathbf{i} + v\mathbf{j} + w\mathbf{k}$, where the Reynolds decomposition gives, for every wind component $u = \overline{u} + u'$, $v = \overline{v} + v'$, and $w = w_{LS} + w'$ (when a positive w_{LS} is prescribed below 5 km, but periodic lateral boundary conditions impose $\overline{w} = 0$ otherwise). $\overline{u}$ and $\overline{v}$ are the background wind components.
- We define the vertically averaged intensive variables x over the breeze depth ($h_{b,est}$) as x_b, giving u_b, v_b, u'_b and v'_b for the wind horizontal components and their anomalies.
- We also define the vertical velocity at the breeze height $w'_{h_b} = w'(z = h_{b,est})$.
- We designate as x^s any horizontally smoothed variable over 10 km. From that, we define the breeze wind as the

10 km-horizontally smoothed wind anomalies u'^s_b, v'^s_b and $w'^s_{h_b}$. The 10 km smoothing is indeed necessary to filter out the variability generated by boundary-layer (i) small-scale turbulence and (ii) thermal plumes.

- From the breeze wind, we finally define the breeze horizontal intensity $I_b = \sqrt{(u'^s_b)^2 + (v'^s_b)^2}$, whose maximum value over the domain gives the breeze strength $I_{b,max} = \max(I_b)$. Similarly, we can define the breeze maximum vertical intensity as $I^{vert}_{b,max} = \max(w'^s_{h_b})$.

3.1.3. Breeze geometry

3.1.4. Size

Figure 2 gives an illustration of the breeze wind. In Figure 2(a), its intensity exhibits two local maxima located on both sides of the patch and downstream. These maxima occur in two opposite, distinct breeze fronts. Indeed, the breeze wind components (u'^s_b, v'^s_b) (Figure 2(a)) shows that these breezes are oriented perpendicularly to the background wind $(\overline{u}, \overline{v})$ and in opposite directions. They consist of a convergence flow whose symmetry axis is given by the low-level background wind direction. We then define the breeze size L_b as the distance between the two breeze fronts, indicated by a thick black line in Figure 2(a). In reality, this distance roughly corresponds to the core of the convergent
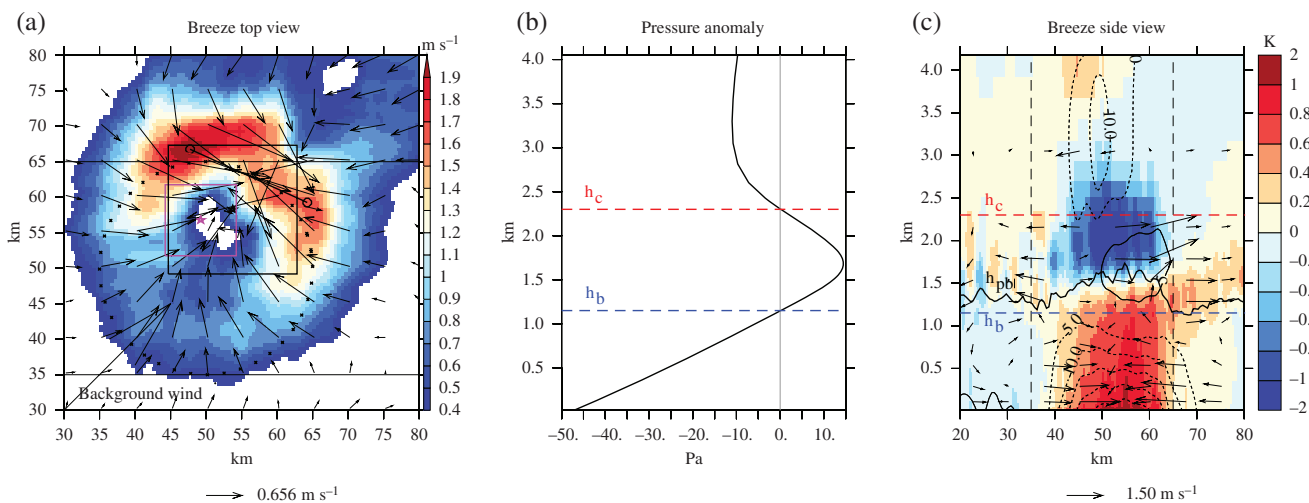
Figure 2. Breeze geometry for the STRONG W0 case at 1200 LT. (a) Breeze top view. Horizontal cross-section of breeze intensity I_b (shading, m s^{-1}) and breeze vectors $(u'^s_b, v'^s_b$, m s^{-1}). The thick black crosses indicate the patch boundaries, the thick black line is the breeze size L_b, the thick black star is the breeze centre $[x_{ctr}, y_{ctr}]$, the black square is the breeze area Ω^{breeze} centred over $[x_{ctr}, y_{ctr}]$ and of size L_b, the thick purple star is the triggering location $[x_{trig}, y_{trig}]$, and the purple square is the triggering zone Ω^{trig}, i.e. a square centred over $[x_{trig}, y_{trig}]$ of 10 km size. (b) Vertical profile of pressure anomaly averaged over the breeze area $\overline{p'^{breeze}}$. (c) Vertical cross-section of potential temperature anomaly θ' (shading, K), wind anomaly vectors (u', v'), pressure anomaly p' (black contours every 5 Pa, negative anomalies dashed) and boundary-layer height h_{pbl} (black line) along the x-axis (longitude). All these variables are averaged in the $y = [35:65]$ km band (see horizontal black lines in (a)). The bold black line is PBL height. Vertical dashed lines indicate the patch boundaries.

mesoscale circulation. In that sense, the denomination 'breeze size' refers to a proxy for the size of the whole mesoscale convective flow (i.e. which consists of an ascending and a subsiding branch). The method employed to compute L_b is described in the Appendix.

3.1.5. Centre

- We define the breeze centre as the position of the minimum surface pressure anomaly over the domain such as $p'_{s,min} = p'(x_{ctr}, y_{ctr})$. The breeze centre is marked with a thick black star in Figure 2(a).
- From the breeze centre, the breeze zone Ω^{breeze} is defined as the L_b-wide square centred at $[x_{ctr}, y_{ctr}]$; it is indicated by the thick black square in Figure 2(a). This zone corresponds to the core of the mesoscale convective circulation, in which convergence is at a maximum.

3.1.6. Height

A first estimate of the breeze depth ($h_{b,est}$) was defined in section 3.1.1. Nevertheless, Figure 2(a) demonstrates that, although the breeze circulation is more or less circular, it does not perfectly match the patch circular shape. As will be detailed later, the breeze circulation is influenced by the low-level monsoon flow that influences the breeze location. The final computation of the breeze height h_b takes into account the exact breeze location, by using the horizontally averaged pressure anomaly field over the breeze zone $\overline{p'^{breeze}}$, where $\Omega^{breeze} = L_b^2$. Then, h_b is the first altitude which verifies $\overline{p'^{breeze}}(z_1 = h_b) = 0$. This height corresponds to the convergence depth of the mesoscale circulation, as illustrated in Figure 2(c). The mesoscale flow converges toward the minimum pressure anomaly $p'_{s,min}$, which also nearly corresponds to the maximum potential temperature anomalies θ'_{max}.

A second altitude of interest is the breeze circulation height h_c which corresponds to the second level (from the surface) where the breeze-averaged pressure anomaly crosses the 0 value (Figure 2(b)):

$$\overline{p'^{breeze}}(z_2 = h_c) = 0 \quad \text{where } z_2 > z_1.$$

h_c is therefore the total height reached by the whole overturning mesoscale circulation, comprising a convergence layer ($0 < z < h_b$), named breeze lower layer, overlaid by a divergence layer ($h_b < z < h_c$), named breeze upper layer. Figure 2(c) illustrates the presence of these two layers, in which air motions are in opposite directions. The low-level convergence sustains a significant ascent which advects low-level θ in the upper breeze layer, leading to a negative anomaly θ' (Figure 2(c)) and the associated positive $\overline{p'^{breeze}}$ in the divergent layer. This divergent flow results in a subsidence whose maximum roughly matches the patch boundaries according to Figure 2(c).

3.2. Thermals and clouds

Several definitions related to thermals and clouds, including their dynamical and geometrical properties are presented below.

- A column hosts a thermal if the vertical velocity is positive at least over the first 250 m: $w'(z) > 0.1 \text{ m s}^{-1}$ for $0 < z < 250$ m. The thermals height is defined as the first level at which vertical velocity decreases below $\epsilon = 0.1 \text{ m s}^{-1}$.
- A column hosts a cloud if at least one of its vertical levels possesses a condensed water mixing ratio $r_c = r_l + r_i$ greater than $10^{-6} \text{ kg kg}^{-1}$, where r_l is the liquid water mixing ratio and r_i is the ice water mixing ratio. In this column, the cloud base h_{base} is defined as the first level

where this condition is verified. The cloud top h_{top} is the first level above cloud base, where the cloudy condition is no longer met.

3.3. Thermodynamical variables

- Similarly to u_b and v_b (section 3.1.2), we define the averaged breeze lower layer potential temperature θ_b, water vapour mixing ratio $r_{v,b}$ and equivalent potential temperature $\theta_{e,b}$, and their anomalies θ'_b, $r'_{v,b}$ and $\theta'_{e,b}$.
- For the breeze upper layer ($h_b < z < h_c$, suffix $_{bc}$), similar definitions are used, giving θ_{bc}, θ'_{bc}, $r_{v,bc}$, $r'_{v,bc}$, $\theta_{e,bc}$ and $\theta'_{e,bc}$.
- For the whole circulation layer ($0 < z < h_c$, suffix $_c$), we get θ_c, θ'_c, $r_{v,c}$, $r'_{v,c}$, $\theta_{e,c}$ and $\theta'_{e,c}$.
- Finally we designate by θ_b^s, $r_{v,b}^s$, $\theta_{e,b}^s$, etc... the 10 km smoothed fields of these variables.

3.4. Triggering definition

Various definitions of deep convection triggering can be found in the literature. According to Rochetin *et al.* (2014a), it corresponds to the rapid growth of a congestus cloud in a cumulus field, inside a given domain. Here, we simply consider that triggering occurs when the highest cloud of the domain $h_{top,max}$ reaches 6 km in height ($h_{top,max} > h_{trig} = 6$ km) for the first time t_{trig} of the simulation, at location $[x_{trig}, y_{trig}]$. The triggering zone Ω^{trig}, is a square of 10 km size centred over $[x_{trig}, y_{trig}]$. In fact, this threshold typically corresponds to the begining of the 'congestus phase', which marks the appearance of the first significant surface rainfall rate, cold pools and, potentially, gravity waves. Our analysis only focuses on the triggering process through boundary-layer thermals and breeze, in the presence of a background wind, i.e. the subtle interaction between these three components and its role in the initial growth of deep cells over a surface flux positive anomaly. It is only after that stage that we observe the formation of cold pools whose dynamics can feedback on deep convection, in broad agreement with Carbone *et al.* (2000), Rieck *et al.* (2014), Hohenegger *et al.* (2015) and Gentine *et al.* (2016).

4. Morphology of the breeze and triggering of deep convection

### 4.1. Time and location of deep convection triggering

Over the Sahel region, according to observations (Taylor *et al.* (2011)), afternoon triggering more likely occurs over dry patches, corresponding to positive surface temperature anomalies. In this section, we analyse the impact of the circular surface heterogeneity on the triggering time and location.

The $h_{top,max}$ time series presented in Figure 3 demonstrates that the presence of a surface sensible heat flux positive anomaly induces an earlier initiation whatever the patch intensity and the magnitude of the large-scale ascent, except for WEAK W0, which reaches h_{trig} but has a similar t_{trig} to HOM. It is worth saying that, for this particular case, clouds do not develop further and even tend to decline right after reaching h_{trig}. For STRONG, the initiation is about 3 h earlier. As expected, for larger positive anomalies, congestus clouds appear 1 h earlier and develop faster, as shown by the comparison between STRONG and WEAK.

The introduction of an afternoon large-scale ascent w_{LS} facilitates deep convection triggering (compare STRONG and STRONG W0 or WEAK and WEAK W0), especially for the WEAK cases. In the STRONG cases, transition is so fast that this ascent has no significant effect on the triggering scenario. However, this ascent helps to sustain deep convection; i.e. $h_{top,max}$ increases again after t_{trig}, while it generally decreases at the end of the simulation for the W0 cases. The absence of a low-level background wind also significantly favours deep convection triggering, which occurs more than 1 h earlier (compare STRONG UV0 and STRONG). This is consistent with previous studies (SA92). Indeed, in the

© 2016 Royal Meteorological Society

Q. J. R. Meteorol. Soc. **143**: 463–478 (2017)
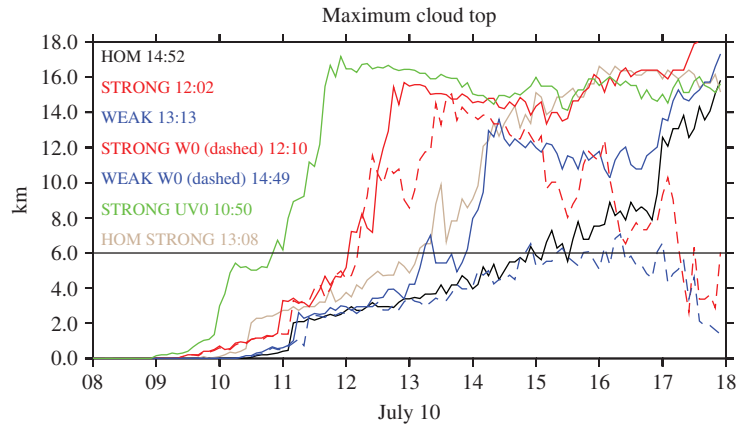
Maximum cloud top

Figure 3. Triggering times: time series of maximum cloud top ($h_{\text{top,max}}$) for seven simulations. The horizontal black line represents the triggering threshold of 6 km. Triggering times (t_{trig}) are listed for each simulation.
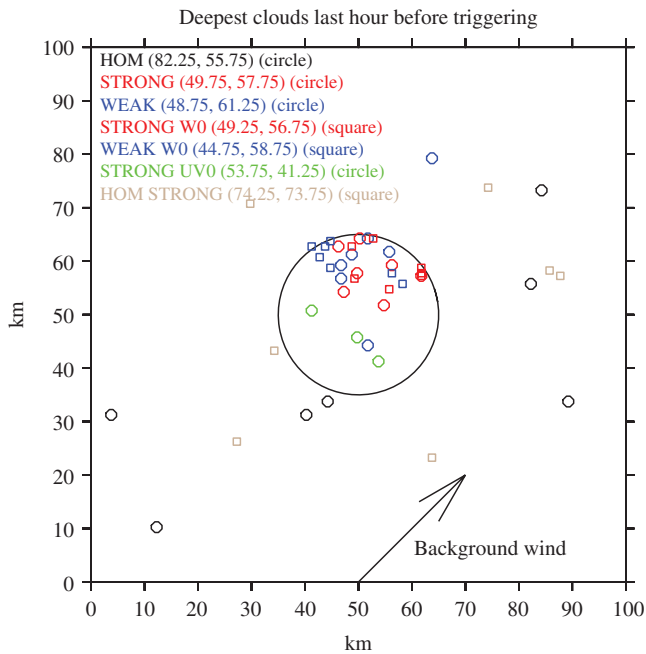
Figure 4. Triggering locations: map of maximum cloud-top locations every 10 min during the last hour before triggering for each case. Co-ordinates of triggering locations [$x_{\text{trig}}, y_{\text{trig}}$] for each simulation are given in the top left corner.

presence of background wind, the pressure gradient induced by the variability of heating at the surface must be strong enough to oppose to it. In addition to that, the background wind smooths the horizontal gradient of low-level potential temperature in the wind direction, which dampens the horizontal breeze strength. Finally, the comparison between HOM and HOM STRONG indicates that a sensible heat flux increase leads to a faster transition and earlier deep convection triggering, consistent with Couvreux *et al.* (2012).

As shown in Figure 4, the presence of a surface heterogeneity strongly determines the triggering location. In all cases with a hot patch at the surface, the deepest clouds prior to triggering are concentrated in a limited area of $\sim 10 \times 10 \, \text{km}^2$ and develop over or close to the patch. In more detail, they are generally shifted downstream relative to the patch centre in the presence of a background wind. This result is consistent with the conclusions raised by Taylor *et al.* (2011) from observations. On the contrary, for the homogeneous cases, the deep convective clouds are more uniformly distributed in space.

In summary, the presence of the surface warm patch fosters the onset of the first congestus clouds which otherwise, over a homogeneous surface, develop more uniformly. The triggering is also faster, and deep convection starts from 1 to 4 h earlier. Thus, the presence of the surface warm patch induces a substantial modification of the temporal and spatial structure of the

convective cloud field and, in the present case, it enhances the spatial aggregation of the moist convective cells. Rochetin *et al.* (2014a,b) have already stressed that triggering time and location can profoundly impact the convection intensity and duration, especially through the thermodynamic state of the atmosphere, which controls the inhibition strength and the rain re-evaporation rate. In the present case, the enhanced degree of aggregation of clouds at triggering may also significantly change the cold pool initial location and dynamics, which partly controls the whole deep convection life cycle.

4.2. Background wind and mesoscale circulations at the time of triggering

Figures 5(a) and (b) presents thermodynamical and dynamical anomaly fields, respectively 1 h before deep convection triggering and at the time of triggering for the STRONG case. One hour before triggering, the potential temperature anomaly in the breeze lower layer (contours of θ'_b in Figure 4(a)) is controlled by (i) the surface fluxes and (ii) the background wind ($\overline{u}, \overline{v}$) (Figures 5(b) and (c)) that advects the temperature anomaly downwind. The maximum θ'_b horizontal gradients are orthogonal to the background wind direction, on the downwind side of the hot patch. Indeed, the background wind advects θ'_b, smoothing the gradients in its direction; this explains the stronger gradient in the orthogonal direction of the background wind. To sum up, the direction of the breeze (u'^s_b, v'^s_b) is roughly aligned with the θ'^s_b horizontal gradient, and thus exhibits an axissymetric structure guided by the background wind, with streamlines oriented perpendicularly to it (black line in Figures 5(a) and (b)). The breeze circulation exhibits a convergence located downstream from the patch centre. It basically matches the θ'^s_b spatial structure, which points to the role of the temperature gradient as a major driver of the mesoscale circulation (identified by the minimum surface pressure anomaly, indicated by a black star in Figures 5(a) and (b) and by the maximum of the smoothed vertical velocity at the altitude h_b, $w'^s_{h_b}$). The ascent strength is a maximum within the breeze area (corresponding to the black square in Figure 5(a)), where convergence is a maximum, while subsidence develops on both sides of the breeze circulation. One hour later, at the time t_{trig}, the breeze circulation has strengthened ($p'_{s,\text{min}}$ decreased, (u'^s_b, v'^s_b) increased) but similar patterns are observed. Nevertheless, θ'^s_b is now weaker, as expected since the surface sensible heat flux has already started its afternoon decrease (Figure 1). The low-level moisture anomaly $r'_{v,b}$ is a maximum on the northern side of the breeze circulation and its spatial distribution becomes more and more skewed with time, with a pronounced maximum on the northern edge of the patch, which is associated with the greater occurrence of deep clouds as shown in Figures 4 and 5(c, d). A physical interpretation of this asymmetric structure will be given in section 5.
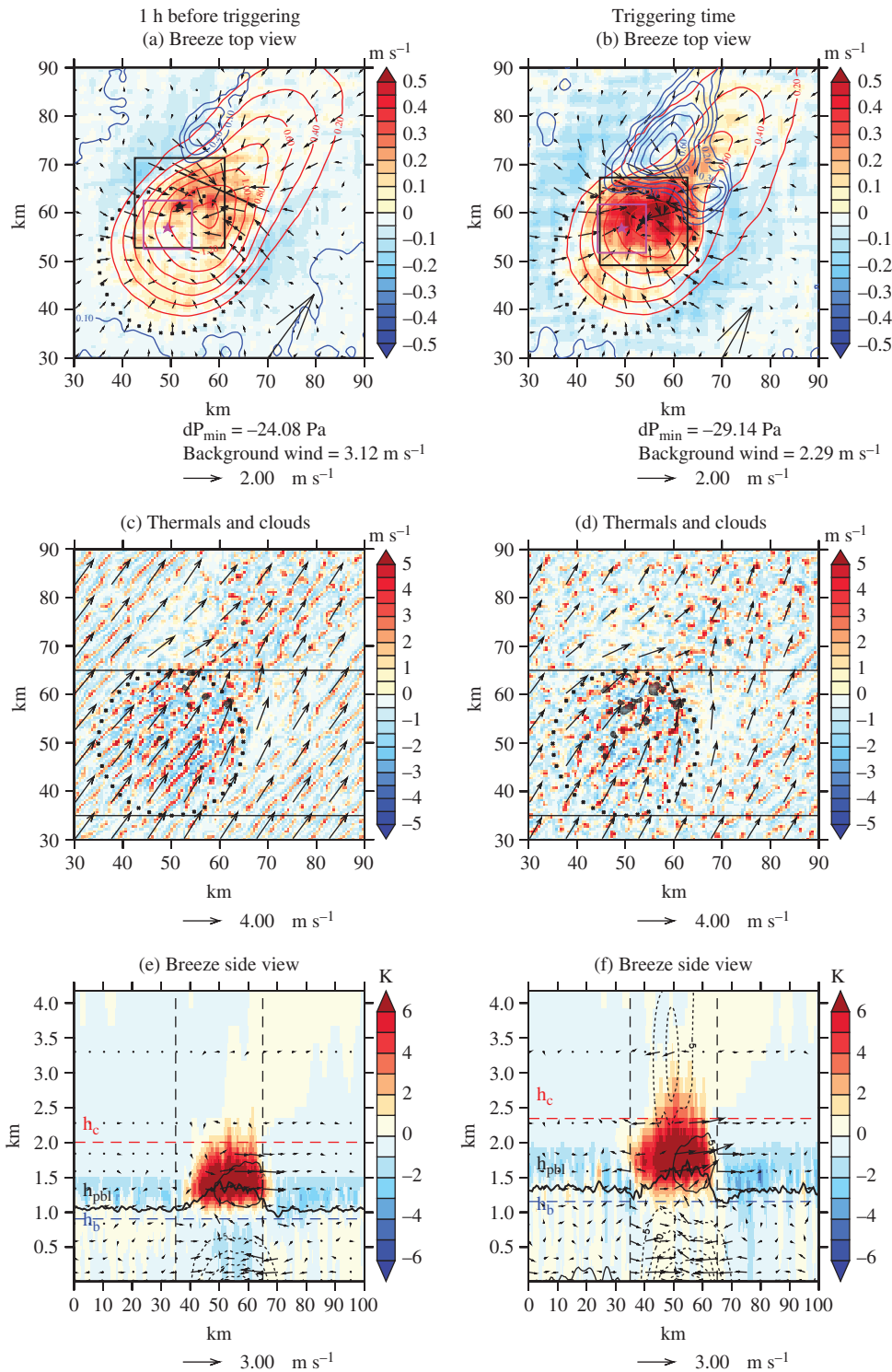
Figure 5. Breeze, thermals and clouds (a, c, e) 1 h before triggering and (b, d, f) at triggering for the STRONG case. (a, b) Horizontal cross-sections of breeze wind vertical velocity $w'^s_{h_b}$ (shading, m s^{-1}), smoothed potential temperature anomaly θ'^s_b (red contours every 0.2 K), smoothed mixing ratio anomaly $r'^s_{v,b}$ (blue contours every 0.1 g kg^{-1}), and breeze vectors (u^s_b, v^s_b, m s^{-1}). The breeze size (L_b), breeze centre (x_{ctr}, y_{ctr}), breeze zone (Ω^{breeze}), triggering location (x_{trig}, y_{trig}) and triggering zone (Ω^{trig}) are displayed as in Figure 2. The low-level background wind vector ($\overline{u_b}, \overline{v_b}$) is shown in the lower right corner, and magnitudes of the minimum surface pressure anomaly $p'_{s,min}$ and of the low-level background wind are given below the panels. (c, d) Horizontal cross-section of vertical velocity w'_{h_b} at breeze height (h_b) (shading, m s^{-1}), liquid water path (LWP, grey filled from 0.1 to 5.1 kg m^{-2}), and smoothed low-level wind vectors (u^s_b, v^s_b). (e, f) Vertical cross-section along x-axis (longitude) of equivalent potential temperature anomaly θ'_e (shading, K), pressure anomaly p' (black contours every 5 Pa, negative values dashed) and wind vectors (u, w) averaged over the $y = [35:65]$ km band (as shown by two black lines in middle panels). The thick black line is PBL height.

Figures 5(c) and (d) show the non-smoothed (i) vertical velocity at the breeze height w'_{h_b}, (ii) the background wind vectors averaged over the breeze height h_b (u_b, v_b) and (iii) clouds. Non-smoothed fields reveals smaller convective structures, like thermals, also at play in the PBL mixing. First, boundary-layer thermals are stronger over the hot patch than everywhere else. One hour before the time of triggering (Figure 5(c)), the spatial structure of w'_{h_b} is closely linked to the pattern of the sensible heat flux anomaly, as expected since the thermal strength is,

at first order, driven by the underlying surface heat fluxes. The spatial organization of thermals is different within the breeze convergence area (black square), where closed cells are found while thermals are generally organized in rolls elsewhere. This is consistent with Weckwerth *et al.* (1999) who show the modification of rolls into cells with increasing instability as measured by z_{rmi}/Lo, Lo being the Monin−Obukhov length; this was also demonstrated for a Sahelian case by Lothon *et al.* (2007). Here, over the breeze convergence the surface heat flux,

and therefore the instability, are stronger. Moreover, a band of stronger thermals, aligned with the direction of the wind convergence, appears on the downstream side of the patch. In the adjacent subsiding regions, thermals are much weaker. Likewise, cloud density and depth are a maximum in the area Ω^{breeze}, in particular near the breeze centre $[x_{\text{ctr}}, y_{\text{ctr}}]$.

Figure 5 further provide a vertical view of the mesoscale circulation and also gives some insights of the thermodynamical structure of the low atmosphere just prior to triggering, especially through the vertical cross-section of θ_{rme}, whose vertical profile is informative of the convective instability of the atmospheric column. The breeze converges towards the minimum pressure zone over the hot patch. The ascending branch of the mesoscale circulation is located near the breeze centre and is associated with a PBL ~ 400 m higher than in the rest of the domain. θ_e is advected from the breeze lower, or convergent, layer to the breeze upper, or divergent, layer in the ascending branch. Interestingly, 1 h before triggering θ_e' is negative in the breeze lower layer. This behaviour is typical of the daytime convective boundary-layer development over semi-arid lands, where the combination of a warmer but drier (in terms of r_v) PBL leads to a negative anomaly of θ_e in the low levels (Guichard *et al.*, 2009; Gounou *et al.*, 2012). This is mainly due to the strength of surface sensible heat fluxes coupled with weak atmospheric lapse rates, which are both major drivers of BL vertical mixing. The positive anomaly θ_e' in the low levels, just prior to t_{trig}, is due to the moisture convergence induced by the breeze circulation, which advects moister air from the surrounding regions into the hot patch. The convergence increases from $t_{\text{trig}} - 1$ h to t_{trig} with a larger negative pressure anomaly. In the breeze upper layer, positive pressure anomalies induce a divergent circulation with associated subsidence motions occurring on both sides of the ascending branch, just over the patch boundaries.

Figure 6 shows that a similar picture is found for the other cases. Triggering occurs generally close to maximum anomaly $\theta_{e,c}'^s$, at similar distances from $\theta_b'^s$ and $r_{v,b}'^s$ maxima. In the WEAK cases, $\theta_b'^s$ and $r_{v,b}'^s$ maxima are closer to each other than in STRONG cases and the triggering zone is shifted on the northern side of the breeze circulation. Without background wind (STRONG UV0), the mesoscale circulation is solely influenced by surface fluxes and strictly matches the patch circular shape. Convergence is a maximum at the centre of the patch and is surrounded by a ring of maximum subsidence motion over the patch boundary. Last, as already stressed in section 4.1, in the absence of surface heterogeneity, triggering is random in space (Figures 4 and 6(f)).

In the following subsections, we focus on the physical processes at play in the transition to deep convection. First, a thermodynamical interpretation is given through the analysis of the properties of the triggering zone until triggering time t_{trig}. Then, a dynamical interpretation is conducted through the analysis of some parameters relative to the breeze geometry and strength during the same period of time.

4.3. Mean thermodynamical properties at the triggering zone

Convective triggering occurs close to the maximum of $\theta_{e,c}'^s$. To further describe the evolution of the thermodynamical properties, we will now examine in more detail the temporal evolution of temperature and moisture in the breeze lower and upper layer.

Positive $\overline{\theta_b'}^{\text{trig}}$ and negative $\overline{\theta_{bc}'}^{\text{trig}}$ (θ_b' and θ_{bc}' averaged over the triggering area) are associated with a higher PBL over the patch (thermals height in Figures 9(a) and (b)), and these anomalies increase with the surface patch strength (Figures 7(a) and (b)). Their time evolution is also strongly controlled by the daytime fluctuations of the sensible heat flux. From 0800 LT until late morning, $\overline{r_{v,b}'}^{\text{trig}}$ decreases while $\overline{r_{v,bc}'}^{\text{trig}}$ increase (Figures 7(c) and (d)). Those anomalies are directly linked to the vertical mixing operated by thermals, which transfer water vapour from the breeze lower to the upper layer. Indeed, the ascending branch

of the mesoscale breeze circulation includes numerous thermals, which together contribute to an enhanced PBL mixing over the patch, as opposed to the impact of the prescribed large-scale ascent which homogeneously moistens the PBL top all across the domain, but at a significantly slower rate. However, in all cases, 1 h prior to triggering, in the low levels, $\overline{r_{v,b}'}^{\text{trig}}$ starts to increase and even becomes positive in WEAK, WEAK W0 and STRONG UV0. This inversion of the trend is due to the breeze-induced moisture convergence, which becomes dominant relative to the drying operated by the thermals.

Time series of $\overline{\theta_{e,b}'}^{\text{trig}}$ and $\overline{\theta_{e,bc}'}^{\text{trig}}$ (Figures 7(e) and (f)) are more complex. First, during the early morning, from 0600 to 0900 LT, $\overline{\theta_{e,b}'}^{\text{trig}}$ increases as the contribution of the potential temperature dominates in the low levels. In a second stage, after 0900 LT, $\overline{\theta_{e,b}'}^{\text{trig}}$ begins to decrease as the rapid PBL growth associated with vigorous thermals transfers the moist static energy excess from the breeze lower layer to the breeze upper layer. This decrease is driven by a strong low-level drying which dominates over the daytime warming. This drying is much less pronounced in the absence of a large-scale wind (STRONG UV0) as the breeze is maximized (it does not need to oppose the mean wind) leading rapidly to convergence of moist air and earlier convective triggering by 1 h. The third phase corresponds to a re-increase of $\overline{\theta_{e,b}'}^{\text{trig}}$ which occurs just prior to t_{trig}. It is primarily explained by the increase of $\overline{r_{v,b}'}^{\text{trig}}$ induced by the low-level moisture convergence. Thus, in all cases, $\overline{\theta_{e,b}'}^{\text{trig}}$ is slightly positive just prior to triggering. In the breeze higher levels, $\overline{\theta_{e,bc}'}^{\text{trig}}$ becomes positive after the mid-morning and its fluctuations seem dominated by the evolution of $\overline{r_{v,bc}'}^{\text{trig}}$. So, at t_{trig}, the whole circulation depth h_c is characterized by $\overline{\theta_{e,c}'}^{\text{trig}}$ positive anomaly.

To sum up, the triggering zone is characterized by (i) a positive heating anomaly due to the presence of the surface hot patch and (ii) a moisture convergence resulting from the breeze circulation. This occurs in such a way that the mesoscale circulation exhibits a significant positive moist static energy anomaly (θ_e) over its whole depth. In this particular zone, surface fluxes and mesoscale processes act together to favour convective cloud development: higher sensible heat fluxes provide more lifting energy to thermals and the low-level moisture convergence feeds deeper clouds. In section 5, we will try to disentangle the respective role of (i) thermals, (ii) breeze and (iii) large-scale wind during the transition to deep convection.

4.4. Breeze characteristics during the transition

The breeze intensity and its time evolution are linked to the strength of the surface flux and pressure anomalies. The stronger the surface anomalies, the earlier the breeze circulation starts and the greater its intensity (Figure 8(a)). This also holds for the intensity of the vertical component of the breeze circulation (Figure 8(b)). The minimum surface pressure (Figure 8(c)) and low-level maximum potential temperature (Figure 8(d)) are also maximized for the larger surface sensible heat flux anomaly. The breeze size L_b ranges from 15 and 35 km. It is larger for WEAK than STRONG cases (Figure 8(e)) and, perhaps surprisingly, systematically shrinks during the morning. An important feature is that the background wind drops from ~ 6 m s^{-1} early in the morning to less than 2 m s^{-1} in the afternoon in all simulations (apart from STRONG UV0 where the background wind is zero). In the case of a zero background wind (i.e STRONG W0), the breeze typical size is close to the patch diameter ($L_b \sim D$). The breeze height h_b and circulation height h_c are positively correlated to the surface perturbation and both monotonically increase before convection triggering (Figure 8(f)). In all cases $h_c \sim 2h_b$ and convective triggering occurs when h_c nearly reaches 2500 m.
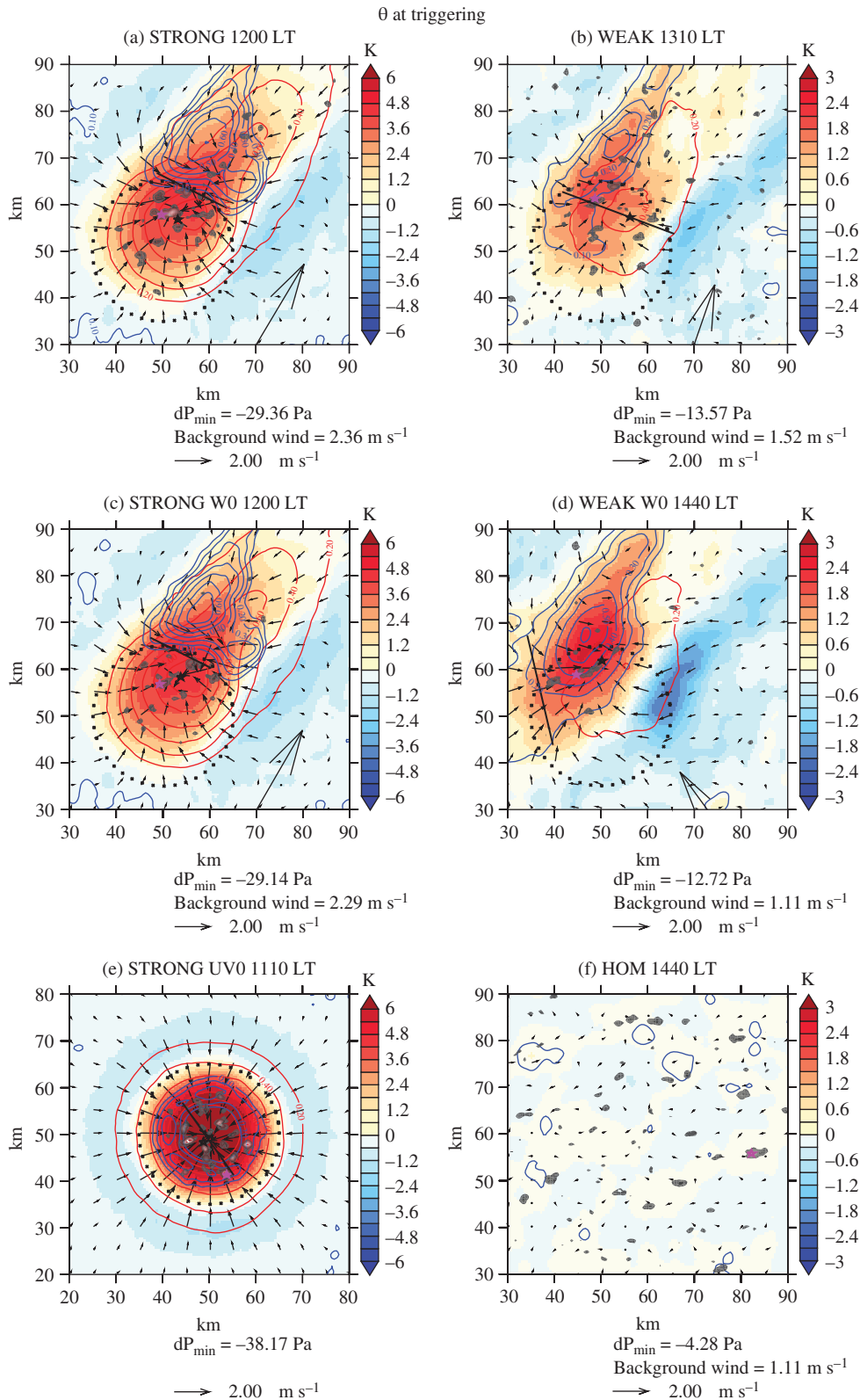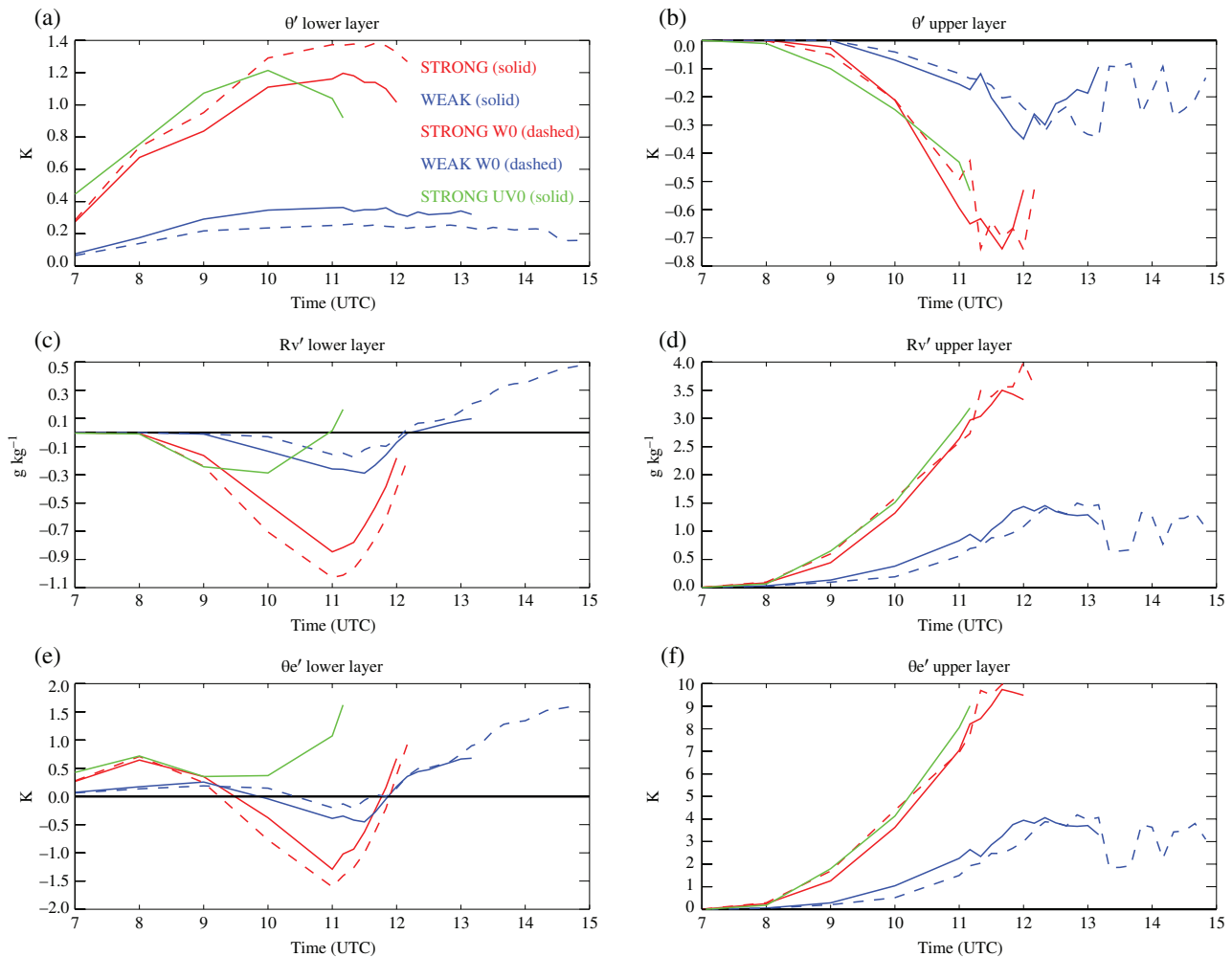
θ at triggering

Figure 6. Breeze circulation at triggering for the (a) STRONG, (b) WEAK, (c) STRONG W0, (d) WEAK W0, (e) STRONG UV0 and (f) HOM cases. Horizontal cross-sections of equivalent potential temperature anomaly $\theta'^{s}_{e,c}$ (shading, K), breeze wind vectors (u'^{s}_{b}, v'^{s}_{b}, m s^{-1}), smoothed potential temperature anomaly θ'^{s}_{b} (red contours every 0.2 K) and clouds (LWP, grey filled from 0.1 to 5.1 kg m^{-2}). Triggering location, breeze horizontal size and patch boundaries are as in Figure 2. The low-level background wind vectors ($\overline{u_b}, \overline{v_b}$, m s^{-1}) are displayed in the lower right corners. Magnitudes of the minimum pressure anomaly $p'_{s,min}$ and of the low-level background wind are given below each panel.

5. The different roles of thermals, breeze and background wind

5.1. Interactions of thermals and breeze circulation

Figure 9 compares the PBL properties over the hot patch and the surrounding area for all the simulations. Not surprisingly, dry and moist convection both develop earlier over the patch than its surroundings. Thermals rise earlier, reach higher levels (Figure 9(a)), are faster and cover a larger fractional area (not shown) of the patch region as larger sensible heat fluxes feeds wider, taller and faster thermals. Cloud depth and fraction are also more important over the patch. An earlier triggering of deep convection is associated with an earlier onset of shallow moist convection. In the surrounding area, thermals and clouds (even though they form earlier) have similar properties compared to

Figure 7. Time series of mean thermodynamical parameters over the triggering zone until triggering averaged over (a, c, e) the breeze lower layer and (b, d, f) the breeze upper layer for the STRONG (red solid), WEAK (blue solid), STRONG W0 (red dashed), WEAK W0 (blue dashed) and STRONG UV0 (green solid) cases. (a, b) Potential temperature anomalies (K) (a) $\overline{\theta'^{trig}_b}$ and (b) $\overline{\theta'^{trig}_{bc}}$. (c, d) Mixing ratio anomalies (g kg^{-1}) (c) $\overline{r'^{trig}_{v,b}}$ and (d) $\overline{r'^{trig}_{v,bc}}$. (e, f) Equivalent potential temperature anomalies (K) (e) $\overline{\theta'^{trig}_{e,b}}$ and (f) $\overline{\theta'^{trig}_{e,bc}}$.

those simulated over a homogeneous surface (Figures 9(b), (d) and (f)).

The comparison of the simulations STRONG and HOM STRONG (where a homogeneous sensible heat flux corresponding to the flux applied over the hot patch is prescribed) indicates that the breeze produces smaller and slower (not shown) thermals but larger cloud fraction. Indeed, the breeze convergence cools and moistens the PBL over the patch by advection. Here the combination of these effects tends to weaken the strength of the boundary-layer dry convection and to favour the development of moist convective clouds. Finally, the convective triggering is significantly advanced (by 1−2 h) in the presence of a breeze, even though the total heat input from the surface is ∼ 40% higher in the HOM STRONG case (Table 1). Thus, not only strong surface sensible heat fluxes produce earlier deep convective triggering, but also the mesoscale breeze circulation happens to play a key role in this process.

Removing the background wind significantly reduces the thermal height and increases the cloud amount over the patch. As mentioned previously, the convergence is stronger in the absence of a background wind and the corresponding breeze circulation is circular. The stronger the breeze, the cooler and moister the PBL overlying the patch will be. Thermals are then weaker but clouds become deeper and wider. This points to a negative influence of the background wind on the breeze strength, via a spreading of the PBL temperature gradients. Without a background wind, the breeze-induced cooling (by horizontal advection) is also slightly stronger (by about 0.1 K) and the maximum moisture convergence coincides with the centre of the

patch. In the surrounding area, thermals are also smaller, possibly linked to the reduced shear-driven turbulence in that case (Pino *et al.*, 2003).

Finally, the large-scale ascent does not affect thermal heights and cloud depths much but induces a substantial increases of the cloud fraction (Figure 9(f)). Indeed, in STRONG and WEAK, this ascent is introduced at noon over the [1, 5 km] layer, and it is much weaker (1.5 cm s^{-1}) than the breeze vertical velocity (Figure 8(b)). Its main effect is to moisten the PBL top and the lower free troposphere without much impact on thermal properties. Conversely, since cloud formation is primarily sensitive to relative humidity, the large-scale ascent substantially enhances the cloud fraction (it roughly doubles from WEAK W0 to WEAK (Figure 9(e)).

To sum up, thermals are mainly controlled by the surface sensible heat flux pattern while clouds are more sensitive to the distribution of low-level humidity. In the presence of a mesoscale surface sensible heat flux anomaly, the induced secondary circulation (breeze) contributes to cool and moisten the hottest PBL. Thus, the breeze weakens the thermals but favours cloud formation through low-level convergence of cooler and moister air. Without background wind, the mesoscale circulation is circular and the low-level heat and moisture anomalies are collocated. The background wind induces a weakening of the convergence induced by the breeze and a delay in the timing of convective triggering. In that latter case, the mesoscale dynamics, driven by the combination of the large-scale wind field and the breeze, generates a mixing ratio positive anomaly which is no longer collocated with the temperature anomaly but shifted
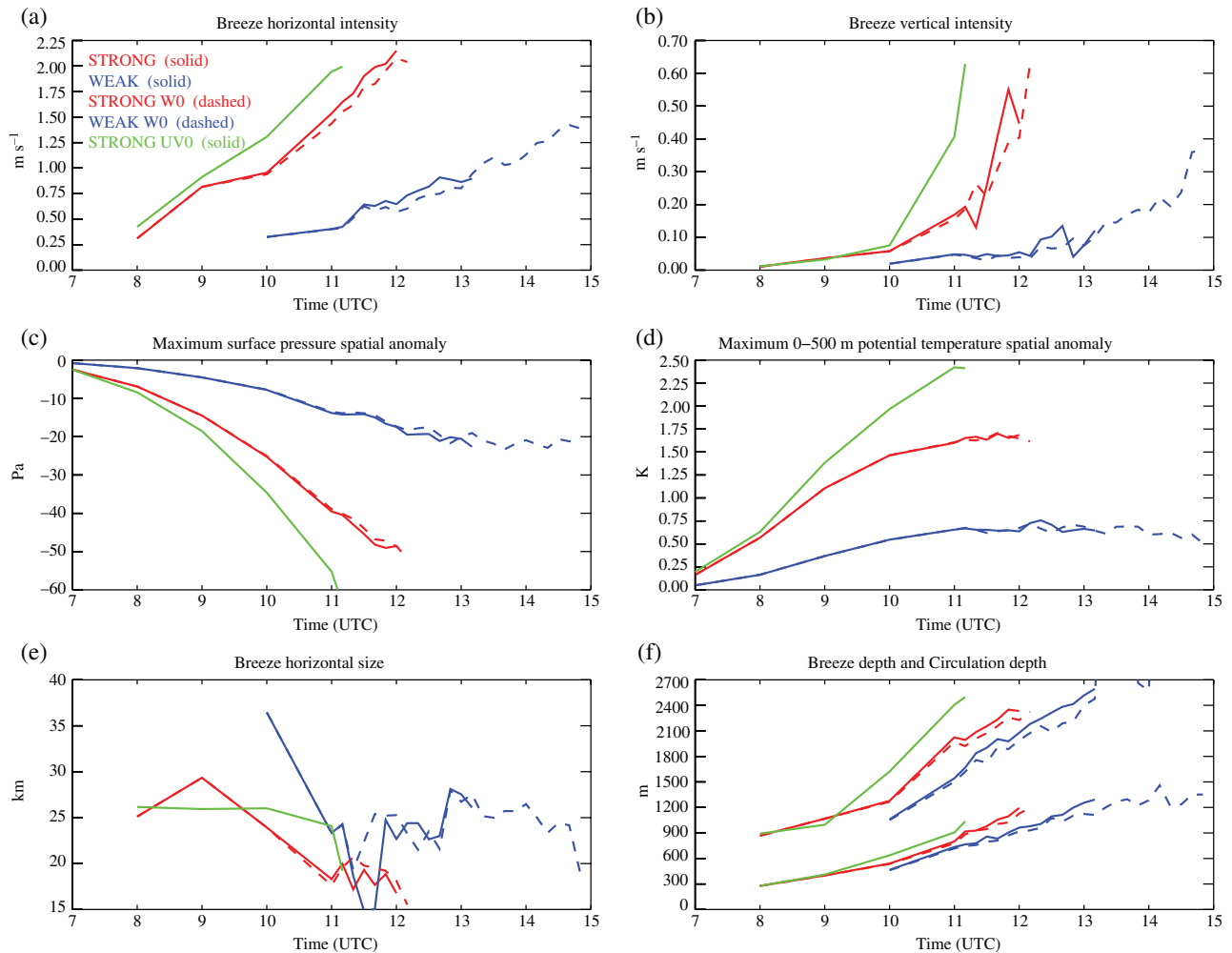
Figure 8. Time series of breeze geometrical, dynamical and thermodynamical parameters until triggering for the STRONG (red solid), WEAK (blue solid), STRONG W0 (red dashed), WEAK W0 (blue dashed) and STRONG UV0 (green solid) cases. Breeze (a) horizontal intensity (m s^{-1}), (b) vertical intensity (m s^{-1}), (c) minimum surface pressure anomaly $p'_{s,min}$ (Pa), (d) maximum 0–500 m averaged potential temperature anomaly θ'_{0-500} (K), (e) breeze size L_b (m) and (f) breeze lower-layer depth h_b (lower lines) and circulation depth h_c (upper lines).

downstream from the patch (Figures 5 and 6). As a result, clouds are then more equally distributed on both sides of the patch boundary, while thermals are generally stronger just over the patch. Consequently, differences in height and depth between clouds located over the patch and outside it are less prominent than for thermals (Figures 9(c) and (d)).

5.2. Modifications of the breeze by the background wind

Consistent with Figures 5 and 6, in all cases where a larger-scale background wind is present, the θ'^s_b anomalies always exhibit an elliptic shape stretched along the background wind direction, though with some subtle differences that are discussed below. The larger-scale background wind stretches the breeze circulation, and therefore weakens the θ'^s_b horizontal gradient, in the wind direction. Consequently, θ'^s_b largest gradients are oriented perpendicularly to the background wind.

From Figure 10, three different stages can be isolated. In the early morning (at 0900 LT, Figure 10(a)) the breeze is very much altered by the background wind. It is stretched along the mean wind vector $(\overline{u_b}, \overline{v_b})$ direction, with a unique breeze front (i.e. a single local maximum of I_b) where the breeze field is roughly aligned with background wind rather than with the θ'^s_b horizontal gradient. In the early morning, the temperature gradients are still weak while the low-level background wind is moderate (~ 4 m s^{-1}). Hence the breeze at 0900 LT is strongly influenced by the low-level background wind. The breeze in the orthogonal direction is weaker although the local heating gradient is the strongest in this direction.

Later in the morning (from 1000 to 1100 LT, Figures 10(b) and (c)) the surface heat flux and the temperature gradients increase substantially. The surface heat flux largely accounts for the PBL rise, which is accompanied by a strong mixing of heat and momentum. This vertical transport of momentum mixes the low-level southwesterly monsoon flow with easterly winds as the PBL rises, thus decreasing its velocity (until less than 3 m s^{-1}): this diurnal fluctuation of the low-level wind is very typical in the Sahel (e.g. Parker *et al.*, 2005). At the same time, the strengthening of the temperature gradients reinforces the secondary circulation, which adopts a more circular shape, while the breeze front splits into two distinct branches. In fact the shape of the secondary circulation is becoming more directly coupled to the temperature gradients. Indeed, both I_b (breeze intensity) and ϕ (breeze orientation) fields responds to the θ'^s_b gradient field. The background wind dilutes the horizontal gradients along the mean direction of the flow so that maximum gradients are now located on both sides of the warm patch. As a result the breeze circulation progressively strengthens in the mean-wind perpendicular direction. In this situation, characterized by a weak low-level background wind, the breeze circular circulation matches the horizontal gradient both in terms of intensity and direction. If the background wind is removed (STRONG UV0), the breeze is everywhere aligned to the gradient (Figure 10(e)).

From 1100 LT, the two breeze fronts start to re-connect into a single overturning circulation (Figure 10(d)). While the breeze strengthens and gets more and more circular, its northern side become stronger than its southern side. The clouds are also slightly shifted northwards, consistently with Figure 4. At 1200 LT, getting closer to the breeze centre, in the wind orthogonal direction, a
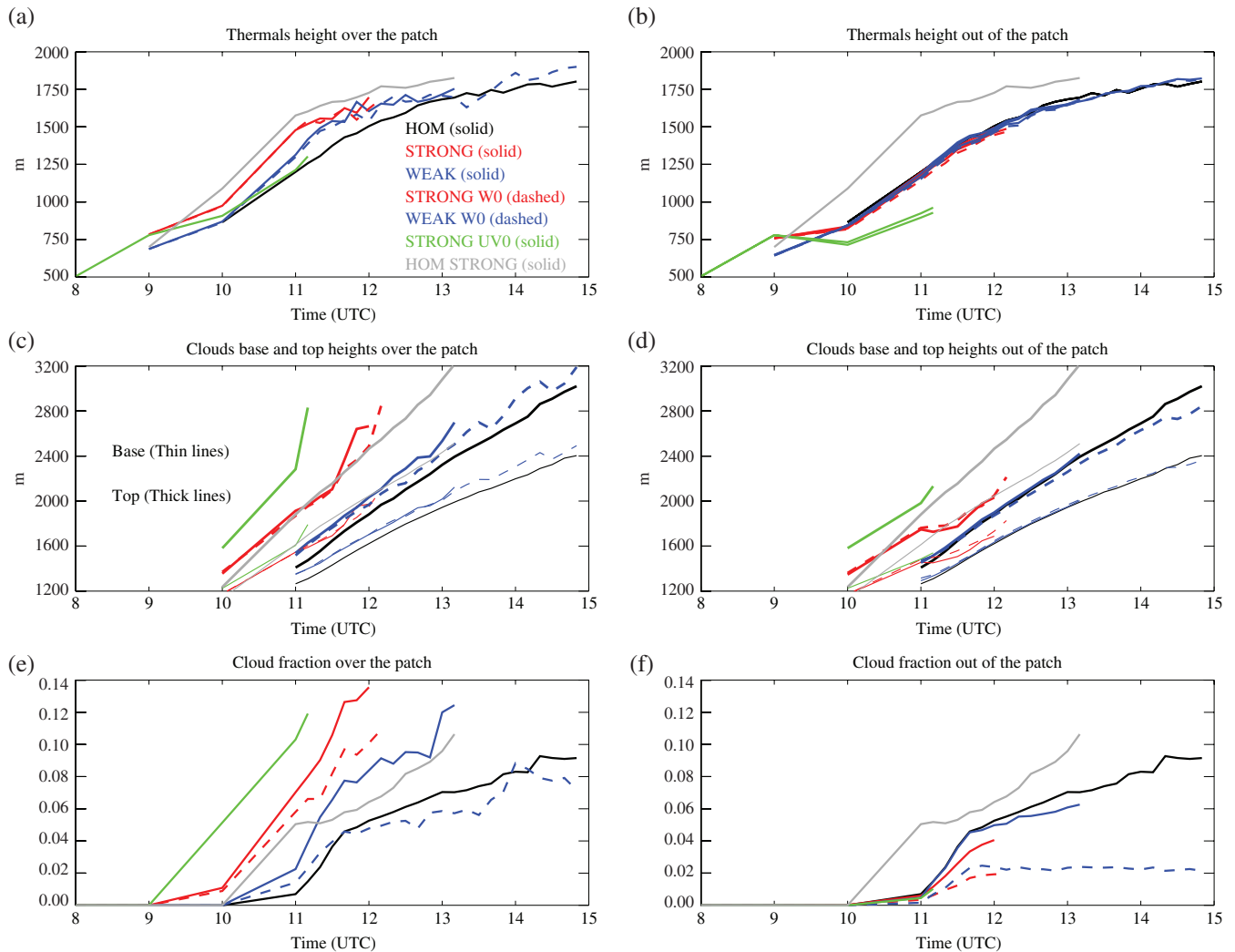
Figure 9. Time series of thermals and clouds parameters (a, c, e) inside and (b, d, f) outside the patch for the HOM (black solid), HOM STRONG (grey solid), STRONG (red solid), WEAK (blue solid), STRONG W0 (red dashed), WEAK W0 (blue dashed) and STRONG UV0 (green solid) cases. (a, b) Thermal height $\overline{h_{th}}$, (c, d) heights of cloud base $\overline{h_{base}}$ (thin lines) and cloud top $\overline{h_{top}}$ (thick lines), and (e, f) cloud fraction.

closed convective circulation issuing from the junction of the two breeze fronts is at play and the breeze vectors $(u_b'^s, v_b'^s)$ are no longer directed solely by the $\theta_b'^s$ gradient. After 1100 LT, an asymmetry develops between the two breeze fronts with a stronger front to the north, contrary to the STRONG NOSHEAR case (Figure 10(f)); a physical interpretation of this asymmetry is proposed in the next subsection.

A similar scenario is observed in all simulations listed in Table 1 as well as in other complementary experiments (not shown), regardless of differences in surface fluxes, hot patch dimensions and even in the absence of cloud (i.e. when water phase changes are ignored, not shown). Indeed, even though clouds could be expected to enhance the breeze circulation via latent heat release as shown by Rieck *et al.* (2015), our simulations did not demonstrate any significant influence of this process on the breeze morphology. Another mechanism through which clouds could potentially affect the breeze circulation is via interactions between the cloud cover and the surface energy budget, but this was not considered in this simulation.

Figure 11 illustrates in a more quantitative way the spatial coherence of I_b with $\theta_b'^s$ along the breeze direction, i.e. the projection of $\theta_b'^s$ gradient onto I_b direction $\left(\sqrt{(\partial\theta_b'^s/\partial x)^2 + (\partial\theta_b'^s/\partial y)^2}\cos(\mathbf{i}\partial\theta_b'^s/\partial x + \mathbf{j}\partial\theta_b'^s/\partial y; u_b'^s\mathbf{i} + v_b'^s\mathbf{j})\right)$ *versus* I_b. Figure 11 basically shows that breeze intensity increases linearly with the magnitude of the local gradient, which is somehow consistent with theory. However, later in the day, the trend increases; that is, for a similar local gradient, the breeze gets stronger. This is due to (i) the mesoscale temperature gradient

increase that accompanies the surface fluxes increase all through the morning (Figure 8(d)) and (ii) the time response of the breeze to a mesoscale heating gradient. Indeed, getting back to Figures 8(a) and (d), one can notice that, even though the heating gradient tends to stabilize around noon, breeze intensity still increases. This time lag corresponds to an adjustment time needed for the breeze to reach its equilibrium relative to the mesoscale heating gradient. In the absence of background wind, this spatial dependency is maximized because there is no dissipation and the breeze fully responds to the gradient. One can also notice a plateau in the rise of the maximum gradient value when getting closer to the triggering time (Figure 11(a)). This plateau just materializes the strong convergence zone at the centre of the overturning circulation, in which strong local temperature gradients are present, but where convergent motions dampen the acceleration.

5.3. Further investigation of the afternoon breeze asymmetry: the role of wind shear

In this subsection, we propose a physical interpretation linking the $r_{v,b}'^s$ and I_b asymmetries that were previously mentioned (sections 4.2 and 5.2) in the presence of the lower tropospheric vertical wind shear below the AEJ. Here, we use the simulation STRONG NOSHEAR corresponding to a simulation without vertical wind shear (Table 1).

In all previous simulations, once the breeze upper layer reached 1800 m, it starts to be affected by the shear of the lower branch of the AEJ. For example, for STRONG, this occurs at 1130 LT. At
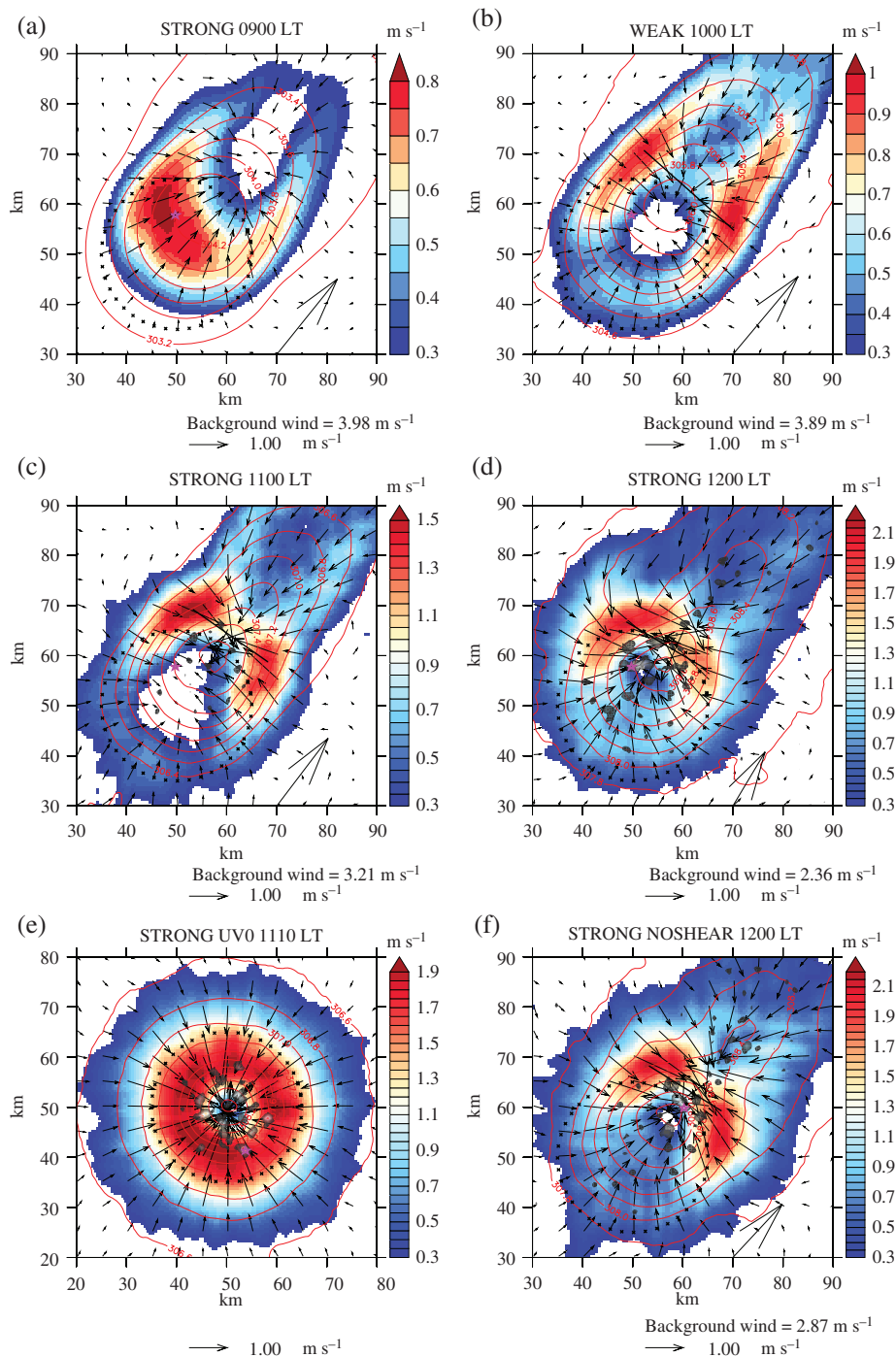
Figure 10. Breeze circulation for (a–d) the last 4 h until triggering for the STRONG case, and at triggering for the (e) STRONG UV0 and (f) STRONG NOSHEAR cases. Horizontal cross-section of breeze intensity (shading, m s^{-1}), breeze vectors (u_b^{ls}, v_b^{ls}, m s^{-1}), smoothed potential temperature θ_b^s (red contours every 0.2 K), and clouds (LWP, grey filled from 0.1 to 5.1 kg m^{-2}). Black crosses thick black line and purple star are as in Figure 2. The low-level background wind vectors ($\overline{u_b}$, $\overline{v_b}$, m s^{-1}) are displayed in the lower right corner and the magnitude below each panel.

the same time, a positive moisture anomaly of 0.6 g kg^{-1} appears in the breeze lower layer on the northwestern side by noon (Figure 12(a)). Later on, this anomaly expands horizontally until reaching the northwestern boundary of the patch. This is also where deeper clouds develop just prior to the triggering of deep convection. By contrast, Figure 12(c) shows that, in the absence of wind shear, clouds are equally distributed on both sides of the wind direction axis, and triggering occurs on this symmetry axis. Moreover, in the absence of shear, the intensity of the breeze I_b is less asymmetric as well. A stronger vorticity appears on the northern side of the patch (Figure 12(b)) in the presence of wind shear, while both subsiding branches are quasi-symmetric without it (Figure 12(d)). Consistently with Froidevaux *et al.* (2014), the interaction between the breeze and the wind shear thus enhances vorticity in the downshear direction.

The sensitivity to the wind shear is also evident in the pressure anomaly and water vapour mixing ratio. We suggest here that the dynamic interaction between the breeze-induced divergent flow in the low free troposphere and the lower branch of the AEJ leads to a more extended positive pressure anomaly in the upshear direction (Figure 12(a)). This pressure force spatial distribution favours penetrative subsiding motions closer to the convergence zone that in the upshear side of it (Figure 12(b)). These subsiding motions favours PBL drying in the upshear direction and results in the simulated low-level humidity and cloud asymmetry.

Thus, the wind shear appears to be an important parameter for the determination of the precise triggering location. The triggering location occurs downstream from the patch centre but is also shifted in the downshear direction. This mechanism suggests an important role of the low-level water vapour heterogeneity pattern. Wind shear thus adds a supplementary dynamical

Theta gradient *versus* Breeze intensity
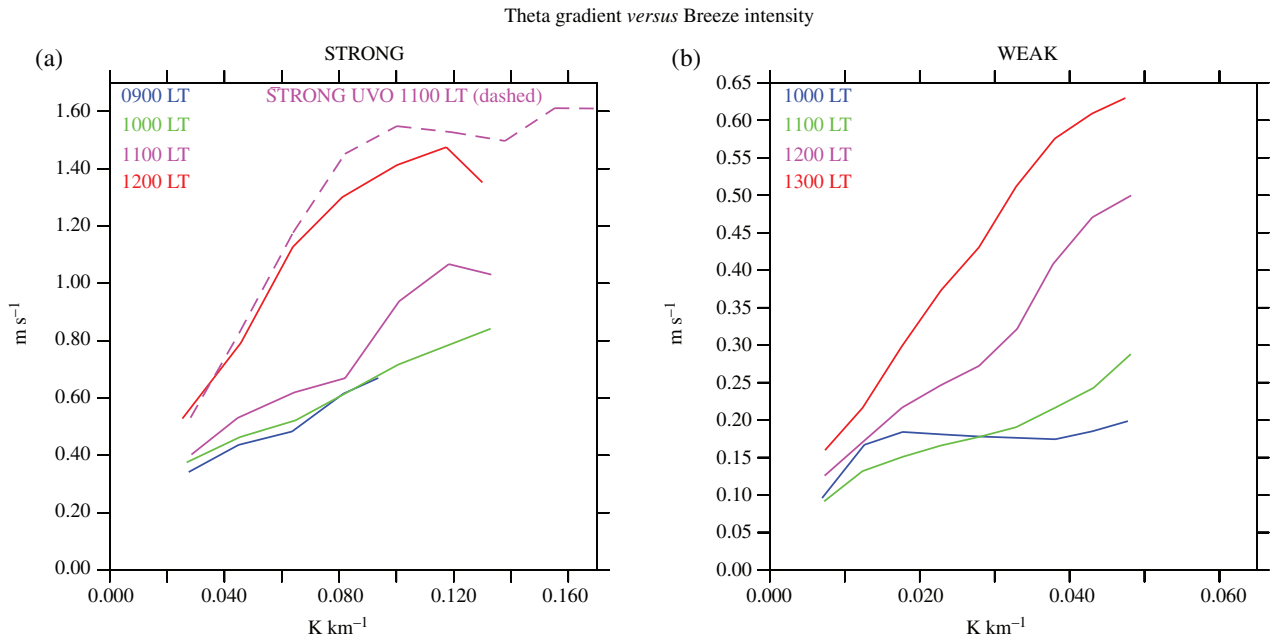
Figure 11. Time evolution of the breeze horizontal intensity (m s^{-1}) as a function of the breeze lower layer potential temperature gradient (K km^{-1}) projected onto the breeze wind direction for the (a) STRONG and (b) WEAK cases. The STRONG UV0 case at triggering is also displayed as an asymptotic STRONG case.
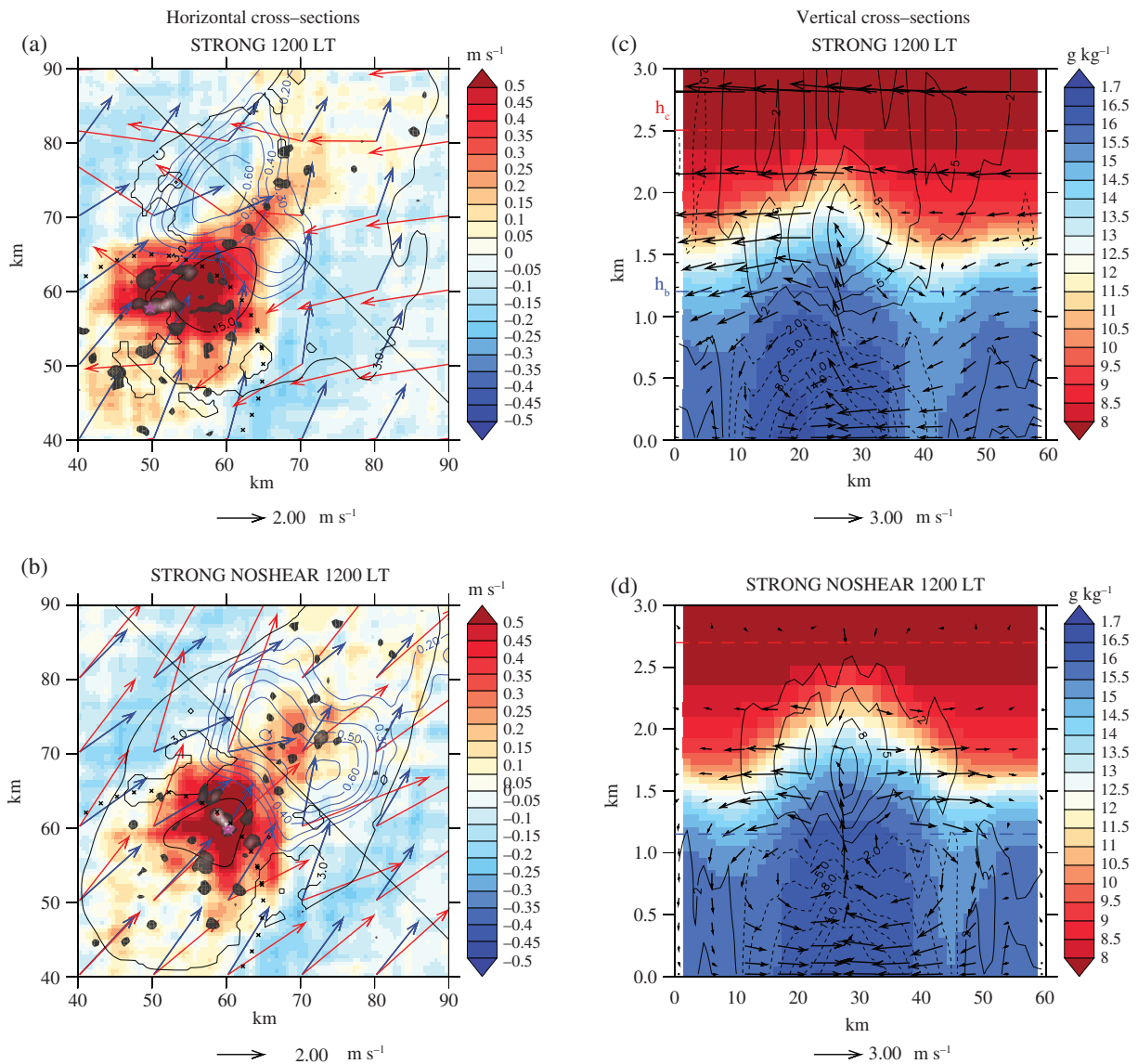
Figure 12. Sensitivity of the breeze structure to the wind shear for the (a, b) STRONG and (c, d) STRONG NOSHEAR cases at triggering (1200 LT). (a, c) Horizontal cross-sections of breeze vertical velocity $w^{\prime s}_{h_b}$ (shading, m s^{-1}), mixing ratio anomaly $r^{\prime s}_{v,b}$ (blue contours, g kg^{-1}), pressure anomaly $p' = 3$ Pa in the breeze upper layer (black contours), lower layer smoothed wind vectors (u^s_b, v^s_b) (blue) and upper layer wind vectors (u^s_{bc}, v^s_{bc}) (red), and clouds (LWP, grey filled from 0.1 to 5.1 kg m^2). Black crosses and purple star are as in Figure 2. (b, d) Vertical cross-sections along the $[x = 45 : 90, y = 90 : 45]$ transect (shown by the black line on (a, c)) of the smoothed wind projected into the transect direction, pressure anomaly p'_s (black contours every 3 Pa) and mixing ratio r_v (shading, g kg^{-1}).

response to the thermal forcing that feeds the breeze circulation. When the breeze layer becomes sufficiently high to interact with the wind shear, an asymmetrical distribution of the pressure forces appears and favours moisture convergence in the downshear direction.

6. Conclusion

In the present study, we analyse the impact of a surface flux heterogeneity on the initiation of daytime convection, encompassing its influence on the structure of the lower atmosphere mesoscale and convective dynamics, from the formation of a breeze to the triggering of deep convection. We focus on a convective event that was observed in a semi-arid Sahelian environment (Lothon *et al.*, 2011) and simulated with large-eddy simulations (Couvreux *et al.*, 2012) and a single-column version of atmospheric climate models (Couvreux *et al.*, 2015). This work relies on these previous studies. In particular, observations suggested an influence of a positive surface sensible heat flux anomaly on the development of this event. Here, a surface flux anomaly, whose shape, size and magnitude are roughly guided by observations, is introduced in the LES. A set of complementary simulations is used to disentangle the processes and mechanisms at play in this observed case of convective triggering in the vicinity of a surface flux anomaly. In particular, the interaction of the surface-induced mesoscale dynamics with the background wind and boundary-layer convection (thermals) is explored. Several mesoscale variables are defined to better describe the daytime transition to deep convection from dynamical, thermodynamical and morphological perspectives.

The introduction of the surface heterogeneity leads to an earlier convective triggering (by 1–4 h depending on the intensity of the patch anomaly) and induces a strong determinism on the triggering location at this scale (i.e. within the $100 \times 100 \, \text{km}^2$ domain of the simulation). More precisely, and in line with observations (Taylor *et al.*, 2011), the convective triggering occurs on the dry side of the surface flux gradient, very close to the patch downstream boundary. Indeed, 1 h before, the deepest clouds all concentrate within a $10 \times 10 \, \text{km}^2$ area. This dramatically contrasts with the random distribution of deep clouds over a homogeneous surface. Thus, the surface flux heterogeneity not only accelerates the convective triggering but also profoundly affects the spatial structure of the simulated deep convective field or, in other words, its organization at the mesoscale. We conducted similar experiments with patches of 20 and 40 km of diameter and found similar results (not shown).

On the thermodynamical side, convective triggering always occurs over the maximum of moist static energy anomaly. The thermodynamic state of the triggering zone is successively driven by (i) turbulent diffusion near the surface, (ii) boundary-layer thermals and (iii) mesoscale circulations that drive moisture convergence and deeper clouds in this area. Everything else being equal, the breeze circulation cools, moistens and then (i) decreases PBL height but (ii) favours cloud formation over the heated patch. The large-scale low-level wind favours the boundary-layer growth and the vertical extent of thermals (Pino and Guerau De Arellano, 2008) by enhancing turbulence while it weakens the breeze intensity by spreading and diluting it. The morphology of the breeze is first shaped by the mesoscale surface pressure perturbation. However, in more detail, the convective triggering can be decomposed into three successive stages which can be interpreted by a subtle balance between the mesoscale pressure gradient and the large-scale wind. Through the day, the breeze intensity and direction is successively dominated by (i) the low-level large-scale wind, (ii) the horizontal temperature gradients and (iii) the overturning mesoscale circulation itself. At sunrise, the breeze is mainly constrained by the background wind and consists of a single breeze front. A few hours after sunrise, the surface-induced low-level breeze consists of two breeze fronts facing each other and oriented perpendicularly to

the wind direction, where the growing near-surface temperature gradients are less diluted by the background wind. Then, as the wind decreases and the surface fluxes increase, the breeze becomes more and more circular in response to the spatial structure of the horizontal temperature gradients until the two breeze fronts connect to create a single overturning circulation with a positive moisture anomaly due to a strong convergent flow towards the breeze centre.

Finally, the asymmetric shape of the mesoscale breeze is linked to or reinforced by the mid-level wind shear. With shear, stronger low-level winds, low-level moisture and higher clouds concentrate on the downshear side of the circulation. We advocate that the divergent breeze mid-level flow creates a more extended positive pressure anomaly on the upshear side, which is associated with a more extended penetrative subsidence and a stronger low-level drying. On the opposite side, the vorticity is stronger and associated with a positive moisture anomaly, which favours upwards motions and enables the development of faster and deeper thermals. Ultimately, this mechanism induces a slight movement of the breeze circulation in the downshear direction.

The present set of experiments provides additional information and physical understanding of the underlying mechanisms explaining the more frequent deep convection onset observed over hot patches in the Sahel. With a relatively simple large-eddy simulation set-up, we decomposed the daytime breeze formation and initiation of deep convection into distinct stages, each one corresponding to a particular combination of processes. Our results point to the importance of correctly representing mesoscale breeze over land in models, and therefore to the relevance of a specific parametrization of these mesoscale phenomena in global models that do not explicitly simulate them. Such a parametrization could potentially help to improve the simulation of the diurnal cycle of convection over land.

Appendix

Computation of breeze horizontal size

The computation of L_b can be divided in four steps:

1. The first step is to localize the position $(x_{b,max}, y_{b,max})$ of $I_{b,max}$ and we compute the orientation

$$\phi_{b,max} = \arctan\left(\frac{v_{b,max}}{u_{b,max}}\right)$$

of the corresponding breeze vector $\mathbf{U}_{breeze}(x_{b,max}, y_{b,max})$.

2. Then a rotation of $\phi_{b,max}$ is applied to the original orthogonal coordinate system $\mathcal{R}$ to compute the breeze field in the new coordinate system $\mathcal{R}_{\phi_{b,max}}$ using the following formulae which hold for the rotation of a Cartesian coordinate system:

$$\left(u_b'^s\right)_{\mathcal{R}_{\phi_{b,max}}} = u_b'^s \cos(\phi_{b,max}) + v_b'^s \sin(\phi_{b,max}), \quad (A1)$$

$$\left(v_b'^s\right)_{\mathcal{R}_{\phi_{b,max}}} = v_b'^s \cos(\phi_{b,max}) - u_b'^s \sin(\phi_{b,max}). \quad (A2)$$

The new coordinate system has then an *x*-axis aligned to the maximum breeze velocity vector.

3. The following step is to find out the position $\left\{\left(x_{b,umin}\right)_{\mathcal{R}_{\phi_{b,max}}}, \left(y_{b,umin}\right)_{\mathcal{R}_{\phi_{b,max}}}\right\}$ of the breeze vector which contains the minimum u_b' component in the $\mathcal{R}_{\phi_{b,max}}$ coordinate system.

4. Finally, the breeze size is taken as the simple distance between $(x_{b,max}, y_{b,max})$ and $\left\{\left(x_{b,umin}\right)_{\mathcal{R}_{\phi_{b,max}}}, \left(y_{b,umin}\right)_{\mathcal{R}_{\phi_{b,max}}}\right\}$:

$$L_b = \sqrt{\left\{\left(x_{b,umin}\right)_{\mathcal{R}_{\phi_{b,max}}} - x_{b,max}\right\}^2 + \left\{\left(y_{b,umin}\right)_{\mathcal{R}_{\phi_{b,max}}} - y_{b,max}\right\}^2}. \quad (A3)$$

References

Agustí-Panareda A, Beljaars A, Ahlgrimm M, Balsamo G, Bock O, Forbes R, Ghelli A, Guichard F, Köhler M, Meynadier R, Morcrette J-J. 2010. The ECMWF re-analysis for the AMMA observational campaign. *Q. J. R. Meteorol. Soc.* **136**: 1457–1472.

Birch CE, Roberts MJ, Garcia-Carreras L, Ackerley D, Reeder MJ, Lock AP, Schiemann R. 2015. Sea-breeze dynamics and convection initiation: The influence of convective parameterization in weather and climate model biases. *J. Clim.* **28**: 8093–8108.

Carbone R, Wilson J, Keenan T, Hacker J. 2000. Tropical island convection in the absence of significant topography. Part I: Life cycle of diurnally forced convection. *Mon. Weather Rev.* **128**: 3459–3480.

Chen F, Avissar R. 1994a. Impact of land-surface moisture variability on local shallow convective cumulus and precipitation in large-scale models. *J. Appl. Meteorol.* **33**: 1382–1401.

Chen F, Avissar R. 1994b. The impact of land-surface wetness heterogeneity on mesoscale heat fluxes. *J. Appl. Meteorol.* **33**: 1323–1340.

Cheng W, Cotton W. 2004. Sensitivity of a cloud-resolving simulation of the genesis of a mesoscale convective system to horizontal heterogeneities in soil moisture initialization. *J. Hydrometeorol.* **5**: 934–958.

Couvreux F, Rio C, Guichard F, Lothon M, Canut G, Bouniol D, Gounou A. 2012. Initiation of daytime local convection in a semi-arid region analysed with high-resolution simulations and AMMA observations. *Q. J. R. Meteorol. Soc.* **138**: 56–71.

Couvreux F, Roehrig R, Rio C, Lefebvre M-P, Caian M, Komori T, Derbyshire S, Guichard F, Favot F, D'Andrea F, Bechtold P, Gentine P. 2015. Representation of daytime moist convection over the semi-arid Tropics by parametrizations used in climate and meteorological models. *Q. J. R. Meteorol. Soc.* **141**: 2220–2236.

Cuxart J, Bougeault P, Redelsperger J-L. 2000. A turbulence scheme allowing for mesoscale and large-eddy simulations. *Q. J. R. Meteorol. Soc.* **126**: 1–30.

Dalu G, Pielke R. 1993. Vertical heat fluxes generated by mesoscale atmospheric flow induced by thermal inhomogeneities in the PBL. *J. Atmos. Sci.* **50**: 919–926.

Dalu G, Pielke R, Avissar R, Kallos G, Baldi M. 1991. Linear impact of thermal inhomogeneities on mesoscale atmospheric flow with zero synoptic wind. *Ann. Geophys.* **9**: 641–647.

Deardorff JW. 1980. Stratocumulus-capped mixed layers derived from a three-dimensional model. *Boundary-Layer Meteorol.* **18**: 495–527.

Dione C, Lothon M, Badiane D, Campistron B, Couvreux F, Guichard F, Sall S. 2014. Phenomenology of Sahelian convection observed in Niamey during the early monsoon. *Q. J. R. Meteorol. Soc.* **140**: 500–516.

Dixon N, Parker D, Taylor C, Garcia-Carreras L, Harris P, Marsham J, Polcher J, Woolley A. 2013. The effect of background wind on mesoscale circulations above variable soil moisture in the Sahel. *Q. J. R. Meteorol. Soc.* **139**: 1009–1024.

Emori S. 1998. The interaction of cumulus convection with soil moisture distribution: An idealized simulation. *J. Geophys. Res.* **103**: 8873–8884, doi: 10.1029/98JD00426.

Findell K, Eltahir E. 2003. Atmospheric controls on soil moisture–boundary layer interactions. Part I: Framework development. *J. Hydrometeorol.* **4**: 552–569.

Froidevaux P, Schlemmer L, Schmidli J, Langhans W, Schär C. 2014. Influence of the background wind on the local soil moisture–precipitation feedback. *J. Atmos. Sci.* **71**: 782–799.

Gal-Chen T, Somerville RC. 1975. On the use of a coordinate transformation for the solution of the navier-stokes equations. *J. Comput. Phys.* **17**: 209–228.

Garcia-Carreras L, Parker DJ, Marsham JH. 2011. What is the mechanism for the modification of convective cloud distributions by land surface-induced flows? *J. Atmos. Sci.* **68**: 619–634.

Gentine P, Garelli A, Park S-B, Nie J, Torri G, Kuang Z. 2016. Role of surface heat fluxes underneath cold pools. *Geophys. Res. Lett.* **43**: 874–883, doi: 10.1002/2015GL067262.

Gounou A, Guichard F, Couvreux F. 2012. Observations of diurnal cycles over a west African meridional transect: Pre-monsoon and full-monsoon seasons. *Boundary-Layer Meteorol.* **144**: 329–357.

Guichard F, Kergoat L, Mougin E, Timouk F, Baup F, Hiernaux P, Lavenu F. 2009. Surface thermodynamics and radiative budget in the Sahelian gourma: Seasonal and diurnal cycles. *J. Hydrol.* **375**: 161–177.

Guichard F, Kergoat L, Taylor CM, Cappelaere B, Chong M, Cohard J-M, Couvreux F, Dione C, Gounou A, Lohou F, Lothon M. 2012. Interactions entre surface et convection au Sahel. *La Météorologie* AMMA: 25–32, doi: 10.4267/2042/48129.

van Heerwaarden CC, Guerau de Arellano JV. 2008. Relative humidity as an indicator for cloud formation over heterogeneous land surfaces. *J. Atmos. Sci.* **65**: 3263–3277.

van Heerwaarden CC, Mellado JP, De Lozar A. 2014. Scaling laws for the heterogeneously heated free convective boundary layer. *J. Atmos. Sci.* **71**: 3975–4000.

Hohenegger C, Schlemmer L, Silvers L. 2015. Coupling of convection and circulation at various resolutions. *Tellus A* **67**: 26678, doi: 10.3402/tellusa.v67.26678.

Huang H-Y, Margulis SA. 2013. Impact of soil moisture heterogeneity length scale and gradients on daytime coupled land–cloudy boundary layer interactions. *Hydrol. Processes* **27**: 1988–2003.

Koster RD, Dirmeyer PA, Guo ZC, Bonan GB, Chan E, Cox P, Gordon CT, Kanae S, Kowalczyk E, Lawrence D, Liu P, Luo CH, Malyshev S, McAvaney B, Mitchell K, Mocko D, Oki T, Oleson K, Pitman A, Sud YC, Taylor CM, Verseghy D, Vasic R, Xue YK, Yamada T. 2004. Regions of strong coupling between soil moisture and precipitation. *Science* **305**: 1138–1140.

Lafore JP, Stein J, Asencio N, Bougeault P, Ducrocq V, Duron J, Fischer C, Héreil P, Mascart P, Masson V, Pinty JP, Redelsperger JL, Richard E, Vilà-Guerau de Arellano J. 1998. The Meso-NH atmospheric simulation system. Part I: Adiabatic formulation and control simulations. *Ann. Geophys.* **16**: 90–109.

Lee S, Kimura F. 2001. Comparative studies in the local circulations induced by land-use and by topography. *Boundary-Layer Meteorol.* **101**: 157–182.

Lohou F, Patton EG. 2014. Surface energy balance and buoyancy response to shallow cumulus shading. *J. Atmos. Sci.* **71**: 665–682.

Lothon M, Couvreux F, Donier S, Guichard F, Lacarrère P, Lenschow DH, Noilhan J, Sad F. 2007. Impact of coherent eddies on airborne measurements of vertical turbulent fluxes. *Boundary-Layer Meteorol.* **124**: 425–447.

Lothon M, Campistron B, Chong M, Couvreux F, Guichard F, Rio C, Williams E. 2011. Life cycle of a mesoscale circular gust front observed by a C-band doppler radar in west Africa. *Mon. Weather Rev.* **139**: 1370–1388.

Lynn B, Tao W, Wetzel P. 1998. A study of landscape-generated deep moist convection. *Mon. Weather Rev.* **126**: 928–942.

Parker DJ, Burton RR, Diongue-Niang A, Ellis RJ, Felton M, Taylor CM, Thorncroft CD, Bessemoulin P, Tompkins AM. 2005. The diurnal cycle of the west African monsoon circulation. *Q. J. R. Meteorol. Soc.* **131**: 2839–2860.

Patton EG, Sullivan PP, Moeng C-H. 2005. The influence of idealized heterogeneity on wet and dry planetary boundary layers coupled to the land surface. *J. Atmos. Sci.* **62**: 2078–2097.

Pielke R. 2001. Influence of the spatial distribution of vegetation and soils on the prediction of cumulus convective rainfall. *Rev. Geophys.* **39**: 151–177.

Pielke R, Lee T, Dalu G, Snook J, Kittel T. 1991. Nonlinear influence of mesoscale land use on weather and climate. *J. Clim.* **4**: 1053–1069.

Pino D, Guerau De Arellano JV. 2008. Effects of shear in the convective boundary layer: Analysis of the turbulent kinetic energy budget. *Acta Geophys.* **56**: 167–193.

Pino D, Guerau de Arellano JV, Duynkerke PG. 2003. The contribution of shear to the evolution of a convective boundary layer. *J. Atmos. Sci.* **60**: 1913–1926.

Pinty J, Jabouille P. 1998. 'A mixed-phase cloud parameterization for use in mesoscale non-hydrostatic model: Simulations of a squall line and of orographic precipitations'. In *Conference on Cloud Physics*, Everett, WA: 217–220. American Meteorological Society: Boston.

Rieck M, Hohenegger C, van Heerwaarden CC. 2014. The influence of land surface heterogeneities on cloud size development. *Mon. Weather Rev.* **142**: 3830–3846.

Rieck M, Hohenegger C, Gentine P. 2015. The effect of moist convection on thermally induced mesoscale circulations. *Q. J. R. Meteorol. Soc.* **141**: 2418–2428.

Rochetin N, Couvreux F, Grandpeix J-Y, Rio C. 2014a. Deep convection triggering by boundary layer thermals. Part I: LES analysis and stochastic triggering formulation. *J. Atmos. Sci.* **71**: 496–514.

Rochetin N, Grandpeix J-Y, Rio C, Couvreux F. 2014b. Deep convection triggering by boundary-layer thermals. Part II: Stochastic triggering parameterization for the LMDZ GCM. *J. Atmos. Sci.* **71**: 515–538.

Roy SB. 2009. Mesoscale vegetation–atmosphere feedbacks in Amazonia. *J. Geophys. Res.* **114**: D20111, doi: 10.1029/2009JD012001.

Segal M, Arritt R. 1992. Nonclassical mesoscale circulations caused by surface sensible heat-flux gradients. *Bull. Am. Meteorol. Soc.* **73**: 1593–1604.

Stirling A, Petch J. 2004. The impacts of spatial variability on the development of convection. *Q. J. R. Meteorol. Soc.* **130**: 3189–3206.

Taylor CM, Parker DJ, Harris PP. 2007. An observational case study of mesoscale atmospheric circulations induced by soil moisture. *Geophys. Res. Lett.* **34**: L15801, doi: 10.1029/2007GL030572.

Taylor CM, Gounou A, Guichard F, Harris P, Ellis R, Couvreux F, De Kauwe M. 2011. Frequency of Sahelian storm initiation enhanced over mesoscale soil-moisture patterns. *Nat. Geosci.* **4**: 430–433.

Taylor CM, Birch CE, Parker DJ, Dixon N, Guichard F, Nikulin G, Lister G. 2013. Modeling soil moisture-precipitation feedback in the sahel: Importance of spatial scale *versus* convective parameterization. *Geophys. Res. Lett.* **40**: 6213–6218, doi: 10.1002/2013GL058511.

Wang S-Y, Gillies RR. 2011. Observed change in Sahel rainfall, circulations, African easterly waves, and Atlantic hurricanes since 1979. *Int. J. Geophys.* **2011**: 259529, doi: 10.1155/2011/259529.

Weckwerth TM, Horst TW, Wilson JW. 1999. An observational study of the evolution of horizontal convective rolls. *Mon. Weather Rev.* **127**: 2160–2179.